



Delft University of Technology

## Improving printability of limestone-calcined clay-based cementitious materials by using viscosity-modifying admixture

Chen, Yu; Figueiredo, Stefan Chaves; Li, Zhenming; Chang, Ze; Jansen, Koen; Çopuroğlu, Oğuzhan; Schlangen, Erik

DOI

[10.1016/j.cemconres.2020.106040](https://doi.org/10.1016/j.cemconres.2020.106040)

Publication date

2020

Document Version

Final published version

Published in

Cement and Concrete Research

### Citation (APA)

Chen, Y., Figueiredo, S. C., Li, Z., Chang, Z., Jansen, K., Çopuroğlu, O., & Schlangen, E. (2020). Improving printability of limestone-calcined clay-based cementitious materials by using viscosity-modifying admixture. *Cement and Concrete Research*, 132, Article 106040. <https://doi.org/10.1016/j.cemconres.2020.106040>

### Important note

To cite this publication, please use the final published version (if applicable).

Please check the document version above.

### Copyright

Other than for strictly personal use, it is not permitted to download, forward or distribute the text or part of it, without the consent of the author(s) and/or copyright holder(s), unless the work is under an open content license such as Creative Commons.

### Takedown policy

Please contact us and provide details if you believe this document breaches copyrights.

We will remove access to the work immediately and investigate your claim.



# Improving printability of limestone-calcined clay-based cementitious materials by using viscosity-modifying admixture



Yu Chen<sup>a</sup>, Stefan Chaves Figueiredo<sup>a,b</sup>, Zhenming Li<sup>a</sup>, Ze Chang<sup>a</sup>, Koen Jansen<sup>a</sup>,  
Oğuzhan Çopuroğlu<sup>a</sup>, Erik Schlangen<sup>a,\*</sup>

<sup>a</sup> Microlab, Faculty of Civil Engineering and Geosciences, Delft University of Technology, Delft, the Netherlands

<sup>b</sup> Department of the Built Environment, Eindhoven University of Technology, Eindhoven, the Netherlands

## ARTICLE INFO

### Keywords:

3D concrete printing  
Viscosity-modifying admixture  
Limestone and calcined clay  
Sustainability  
Mechanical performance

## ABSTRACT

In 3D concrete printing (3DCP), it is necessary to meet contradicting rheological requirements: high fluidity during pumping and extrusion, and high stability and viscosity at rest to build the layered structure. In this paper, the impact of the hydroxypropyl methylcellulose (HPMC)-based viscosity-modifying admixture (VMA) on the 3D printability and mechanical performance of a limestone and calcined clay based cementitious material is investigated. A combination of VMA and superplasticizer was used for that purpose. In this case, controlling the competitive effects between VMA and superplasticizer becomes critical. The main strategy for 3D printing in this study was to add an optimal dosage of VMA in the solid suspension that was already mixed with water and superplasticizer. A lab-scale 3DCP setup was developed and demonstrated as well. A series of tests was performed to characterize the effects of VMA on flowability, extrudability, open time, buildability, green strength, hydration, compressive strength, and air void content and distribution. Experiments performed in this study showed that the mixture containing 0.24% (of the binder mass) of VMA exhibited satisfactory 3D printability and optimal mechanical performance. Finally, the results, limitations, and perspectives of the current research were discussed.

## 1. Introduction

Additive manufacturing (AM) has been developing rapidly in different fields of science and engineering in the past few decades [1,2]. American Society for Testing and Materials (ASTM F2792-10 [3]) defines AM as “a layer-based process of joining materials to fabricate objects based on 3D model data”. AM technologies have become a daily routine in many industries [2,4], e.g., aerospace, biomedical, and food, among others [4]. In the construction industry, AM of concrete is a natural choice, since concrete is the most widely used construction material worldwide. 3D concrete printing (3DCP), or digital concrete construction, has been under development for the past 20 years with an increasing rate of research and application [5]. Currently, two major 3DCP technologies are under development: extrusion-based and selective binding methods [6,7]. This article focuses on extrusion-based 3DCP. Many companies, such as Contour Crafting, XtreeE, CyBe, Apis Cor, WinSun, and others, attempted to implement extrusion-based 3DCP in practice [8], showing the potential of this technology.

Development of extrusion-based 3DCP could bring massive benefits

to building and construction projects. As illustrated by [5,9,10], extrusion-based 3DCP can eliminate the need for formwork, reduce the required cost and time of construction, increase the safety of construction site and flexibility of architectural design. However, as mentioned by Wangler et al. [11], a relatively high cement content in the mix design of digital concrete is needed to satisfy the rheological requirements during the manufacturing process, neutralizes the benefit of material-efficient designs. For extrusion-based 3DCP, most proposed mixtures contain larger quantities of ordinary Portland cement (OPC) than typical conventionally cast concrete [6,12–14] with similar mechanical performance. It is clear that for 3DCP techniques to become an alternative to current practices, sustainable binders must be developed that are technically capable yet do not compromise sustainability. As the technology matures, researchers now need to develop sustainable cementitious materials by replacing part of OPC with supplementary cementitious materials (SCMs) for extrusion-3DCP. Many common SCMs, such as fly ash, silica fume, and blast-furnace slag, have been involved in many sustainable and 3D printable concrete proposals (see [7–9,15–17]). However, these SCMs are gradually being depleted, and

\* Corresponding author.

E-mail addresses: [Y.Chen-6@tudelft.nl](mailto:Y.Chen-6@tudelft.nl) (Y. Chen), [S.ChavesFigueiredo@tudelft.nl](mailto:S.ChavesFigueiredo@tudelft.nl) (S. Chaves Figueiredo), [Z.Li-2@tudelft.nl](mailto>Z.Li-2@tudelft.nl) (Z. Li), [Z.Chang-1@tudelft.nl](mailto:Z.Chang-1@tudelft.nl) (Z. Chang), [K.Jansen-2@student.tudelft.nl](mailto:K.Jansen-2@student.tudelft.nl) (K. Jansen), [O.Copuroglu@tudelft.nl](mailto>O.Copuroglu@tudelft.nl) (O. Çopuroğlu), [Erik.Schlangen@tudelft.nl](mailto:Erik.Schlangen@tudelft.nl) (E. Schlangen).

we need to look for alternatives.

The limitations of widely utilizing those common SCMs in conventional concrete have been discussed by Scrivener et al. [18]. The authors point out that limestone and calcined clay cement is an appropriate solution for developing sustainable concrete in the longer term. Using calcined clay, especially when clays with a lower kaolinite content (referred as low-grade calcined clay in this paper) are used, in concrete shows remarkable advantages, including: (1) lower CO<sub>2</sub> emissions during the production of calcined clay (about 0.3 kg of CO<sub>2</sub> per kg of calcined clay) [18,19]; (2) worldwide abundance [18,20,21]; (3) comparable early-age strength [13,22,23]; (4) capillary porosity refinement due to the pozzolanic reaction [20,21,24,25]; (5) lower cost [19,26]. Note that, at present, the benefits of using calcined clay in printable concrete might not be that significant since 3DCP is not widely used yet. Nevertheless, given the potential of 3DCP technology, it is worthwhile to provide a more sustainable and economical option for 3DCP. Chen et al. [6] reported that it is possible to develop 3D printable limestone and calcined clay-based cementitious materials. Previous studies [13,27] have looked into the extrudability of several mixtures based on ternary blends (OPC, limestone, and calcined clay) using a ram extruder. However, to our knowledge, a systematic investigation of mix designs and fresh state behaviors of limestone and calcined clay-based cementitious materials for extrusion-based 3DCP has not been performed to date.

The main challenge behind developing 3D printable cementitious materials is to engineer specific fresh properties that will allow for extrusion-based printing. In comparison with cast concrete, the lack of formwork to provide the dimensional stability of fresh materials during the printing process is the main reason for this challenge. Therefore, the fresh mixtures must exhibit low-slump and high-thixotropy to be used in concrete 3D printing [15,28]. Many studies [7,9,11,15,28] have targeted to explore the fresh state behaviors of printable cementitious materials, including extrudability, open time, and buildability. Le et al. [9] proposed a series of tests to develop a high-performance fiber-reinforced cementitious material for 3DCP. Kazemian et al. [29] demonstrated several methods to evaluate the printing quality and shape stability of fresh mixtures. Ma et al. [15] utilized existing test methods to find the optimal mix design of concrete containing copper tailings for 3DCP. Recently, new test methods for quantifying and evaluating the fresh properties of 3D printable cementitious materials have been developed [8,30–34].

It seems paradoxical to expect 3D printable cementitious materials to show proper extrudability and buildability at the same time [35]. A balance between sufficient flowability for extrusion and high green strength after deposition must be found [16,36]. Different performances of fresh mixtures under dynamic and static conditions could be attributed to rheology and thixotropy of cementitious materials. Roussel [37] summarized the required rheological properties of cementitious materials for 3DCP. In general, rheology of concrete depends on the mix design, which is related to volumetric and compositional features (presence of cement, filler, and SCMs) of the binder system, particle shape, content and aggregate gradation, as well as the water to binder ratio [6,12,36]. Furthermore, admixtures, such as superplasticizers, viscosity modifiers, and accelerators, could be employed to tailor the rheological performance [36].

Many printable mixtures developed earlier [8,13,27,29,38] contained both superplasticizer and viscosity-modifying admixture (VMA). Superplasticizer in cementitious materials could contribute to increasing flowability at a constant solids content for facilitating the casting, pumping, and extrusion in 3DCP [36]. A small dosage of VMA has been used to replace the fine content (fly ash, silica fume, or limestone) in self-compacting concrete [39] in order to enhance cohesion, stability, and viscosity [40]. Previous studies [27,38,41] have demonstrated that addition of VMA could significantly improve the printability of solid suspensions through adjusting the yield stress and plastic viscosity. As explained by Reiter et al. [30], VMA could enhance

flocculation of cement grains through providing more contacts and bridges between cement particles, which will promote the evolution of green strength for the deposited layers. VMA can also ensure extrudability since it reduces water drainage of the cementitious materials [38,42].

Hydroxypropyl methylcellulose (HPMC) is one of the most widespread cellulose-derivative VMAs applied in practice [43]. Many studies have attempted to utilize a combination of HPMC and superplasticizer to develop printable cementitious materials [8,29,31,38,44]. However, most of them overlook the fact that the HPMC could compete with superplasticizer to adsorb onto cement or other fine particles, thereby affecting the dispersion of superplasticizer. Besides, the competitive effects between HPMC and superplasticizer in a suspension may increase the yield stress and apparent viscosity, which will result in a significant increase in extrusion pressure. This impact may be suitable for buildability, whereas it adversely affects extrudability. The dosage of VMA becomes very critical in this context. Therefore, this paper proposes a strategy to utilize the HPMC-based VMA for developing limestone and calcined clay-based printable cementitious materials, specifically, by adding an optimal dosage of VMA in the fresh mixture. For developing printable cementitious materials in the laboratory, a lab-scale 3DCP setup was also demonstrated. A series of tests were conducted to investigate the effects of VMA dosages on the fresh state behavior of 3DCP, including flowability, extrudability, open time, buildability, and green strength. Furthermore, the impacts on the hydration, mechanical performance, and air void content were determined via isothermal calorimetry, compressive strength (7 days) testing, and X-ray computed tomography (CT) scanning. Finally, a discussion of the obtained results, including the limitations and perspectives of the current research is presented.

## 2. Material and methods

### 2.1. Raw materials and fresh mixture preparation

Primary cementitious materials used in this study were CEM I 52.5R Portland cement, limestone powder, and low-grade calcined clay. The low-grade calcined clay was manufactured by flash calcination of 50% kaolinite clay from Argeco, France, and contains 40–50 wt% of metakaolin. The chemical composition of raw materials was obtained by X-ray fluorescence spectrometry (XRF) (see Table 1). Fig. 1 gives X-ray diffraction (XRD) patterns of CEM I 52.5R Portland cement, limestone powder, and low-grade calcined clay. XRD was conducted on a PhilipsPW1830 powder X-ray diffractometer, with Cu-K $\alpha$  radiation operated at 45 kV and 40 mA, for 20 values between 5° and 75°. The broad shallow hump appeared at 15–30° 20 in low-grade calcined clay indicated the presence of amorphous phases. Besides, many crystalline phases like mullite (3Al<sub>2</sub>O<sub>3</sub>·2SiO<sub>2</sub>), kaolinite (Al<sub>2</sub>O<sub>3</sub>·2SiO<sub>2</sub>·2H<sub>2</sub>O), and quartz (SiO<sub>2</sub>) were found in low-grade calcined clay. CEM I 52.5R Portland cement was mainly composed of alite (3CaO·SiO<sub>2</sub>), belite (2CaO·SiO<sub>2</sub>), tricalcium aluminate (3CaO·Al<sub>2</sub>O<sub>3</sub>) and gypsum

**Table 1**  
The chemical composition of binder materials, determined by XRF (wt%). Based on internal standards.

Oxide (wt%)	CEM I 52.5R Portland cement	Limestone powder	Low-grade calcined clay
CaO	68.7	39.6	0.6
SiO <sub>2</sub>	17.4	0.2	55.1
Al <sub>2</sub> O <sub>3</sub>	4.1	0	38.4
Fe <sub>2</sub> O <sub>3</sub>	2.8	0.1	2.6
K <sub>2</sub> O	0.6	0	0.2
TiO <sub>2</sub>	0.3	0	1.1
ZrO <sub>2</sub>	0	0	0.1
Other	6.1	60.1	1.9
Total	100.0	100.0	100.0

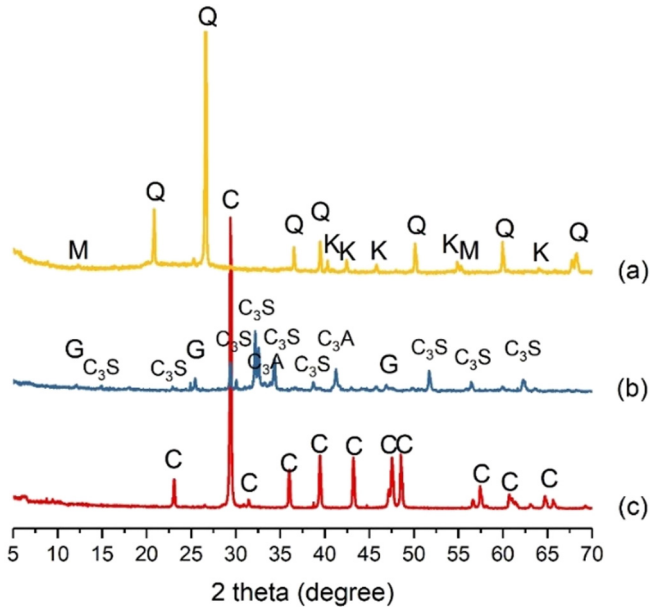


**Fig. 1.** XRD analysis results: (a) Low-grade calcined clay; (b) CEM I 52.5R Portland cement; (c) Limestone powder. M-mullite, Q-quartz, K-kaolinite, G-gypsum,  $\text{C}_3\text{S}$ -alite,  $\text{C}_3\text{A}$ -tricalcium aluminate, C-calcite.

( $\text{CaSO}_4 \cdot 2\text{H}_2\text{O}$ ). Calcite ( $\text{CaCO}_3$ ) was the primary phase found in the limestone powder. According to our earlier study [13], the contents of the reactive  $\text{SiO}_2$  and  $\text{Al}_2\text{O}_3$  in low-grade calcined clay were determined by a chemical dissolution method, and about 48.8 wt% of the amorphous part was found. The molar mass ratio of Si/Al in the reactive part was 0.33. Due to the size limitation of the pump-hose-nozzle system, quartz sand with a maximum diameter of 2 mm was used as aggregate in this study. The cumulative particle size distribution of all dry components is given in Fig. 2.

As stated by Marchon et al. [45] and Lei and Plank [46], the swelling clay-like montmorillonite could consume a large amount of “standard” polycarboxylate ether (PCE)-based superplasticizers which has a conventional polyethylene glycol (PEG) side chain. However, for the non-swelling clay, such as kaolinite, muscovite, and mica, there is no severe impact on the performance of “standard” PCE-based superplasticizers. Therefore, a PCE-based superplasticizer (MasterGlenium®51, BASF) was selected in this study.

To modify the cohesion, viscosity, and water-retaining properties, a hydroxypropyl methylcellulose (HPMC)-based viscosity-modifying admixture (VMA) in powder form was used. It was supplied by Shanghai Ying Jia Industrial Development Co., Ltd. The viscosity of HPMC was

reported by the manufacturer as 201,000 mPa.s. Previous studies have demonstrated the compatibility of cellulose-derivative VMAs with PCE-based superplasticizer [47,48]. However, the competitive adsorption between HPMC and PCE cannot be avoided when both of them are present in the solid suspension. As stated by Palacios and Flatt [48], the addition of cellulose-derived VMAs could increase the plastic viscosity and yield stress with a fixed percentage of superplasticizer.

The mix designs developed by the authors [27] are presented in Table 2. In the current study, all mixture compositions were kept identical except the VMA dosage, which varied from 0 to 0.48% by mass of binder. The binder, which amounted to about 35.5 wt% of the total mass in all mixtures, contained 40 wt% of Portland cement (331 kg/m<sup>3</sup>), 40 wt% of low-grade calcined clay and 20 wt% of limestone. Binder to sand ratio (B/S) was selected as 2/3, in accordance with previous studies [13,27]. After a series of trial and error tests, w/b of 0.3 and 2% of the binder mass of PCE, which could ensure sufficient workability, was selected. The fresh mixtures were prepared using a planetary mixer (HOBART) by following the procedures given in Fig. 3. There were two tracks of the material preparation. Track 1 provided specific steps for the mixture Ref. The mixtures containing VMA were prepared following track 2. The time zero ( $T = 0$  min) was defined as the moment when the suspension (water and PCE) was added to the dry mixture.

## 2.2. Lab-scale 3D concrete printing setup

A lab-scale 3DCP setup was designed and assembled at the Delft University of Technology. As shown in Fig. 4 (a), this system comprises three main parts: a three-degree-of freedom Computer Numerical Control (CNC) machine, a controller (containing a computer), and an extrusion system. The CNC machine, which is operated by the controller, operates within an area of 1100 mm (Length), 720 mm (Width), and 290 mm (Height) frame. Step-motors are employed to ensure the high precision of movement in different axes. The core component of the extrusion system is a commercial PFT Swing-M conveying pump that is a rotor-stator configuration. Fig. 4 (b) gives the schematic diagram of the conveying pump, which includes three parts: a hopper (volume: 38 L), a rotor as well as an extruder with a barrel and a die. A PFT hose with an inner diameter of 25 mm and a length of 5 m is used to connect the die with the conveying pump. A nozzle with a rectangular opening ( $40 \times 13.5 \text{ mm}^2$ ) is connected with the hose and mounted on the end part of the z-axis. This extrusion system is based on the laminar flow printing mechanism. The moving speed of the printing nozzle (nozzle moving speed) can be adjusted between 0 mm/s and 120 mm/s.

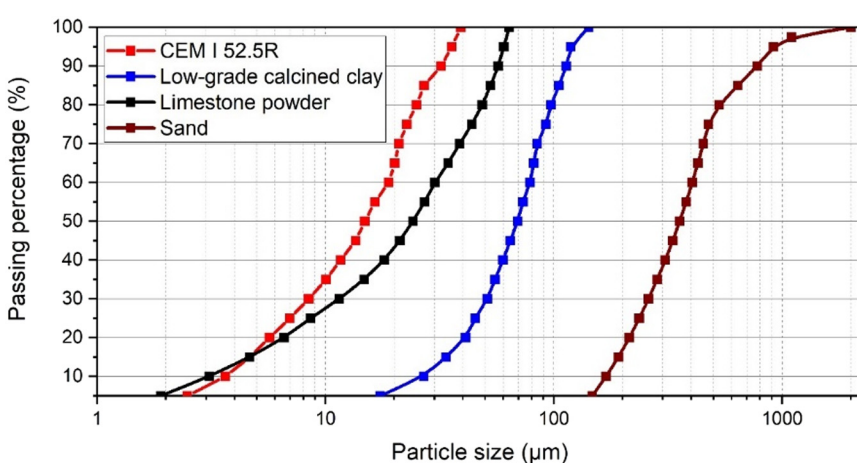


**Fig. 2.** The particle size distribution of all dry components used in 3DCP mix designs. The grain size of sand was measured via the sieving machine. The other dry components were quantified by laser diffractometry.  $D_{50}$  of CEM I 52.5R Portland cement, low-grade calcined clay, and limestone powder was 14.86  $\mu\text{m}$ , 69.35  $\mu\text{m}$ , and 24.19  $\mu\text{m}$ , respectively.

**Table 2**

Mix designs of cementitious materials (% of the binder mass).

Type	Binder		Sand	Water	PCE	VMA	
	CEM I 52.5R Portland cement (wt%)	Low-grade calcined clay (wt%)	Limestone powder (wt%)	(wt%)	(wt%)	(wt%)	(wt%)
Ref	40	40	20	150	30	2	0
1.2VMA	40	40	20	150	30	2	0.14
2VMA	40	40	20	150	30	2	0.24
4VMA	40	40	20	150	30	2	0.48

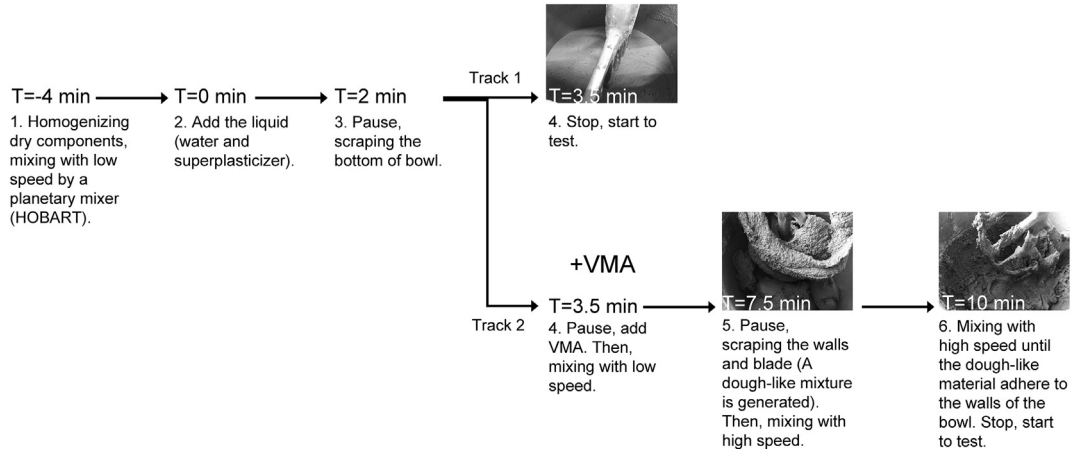


Fig. 3. Mixing procedure for the fresh mixture preparation.

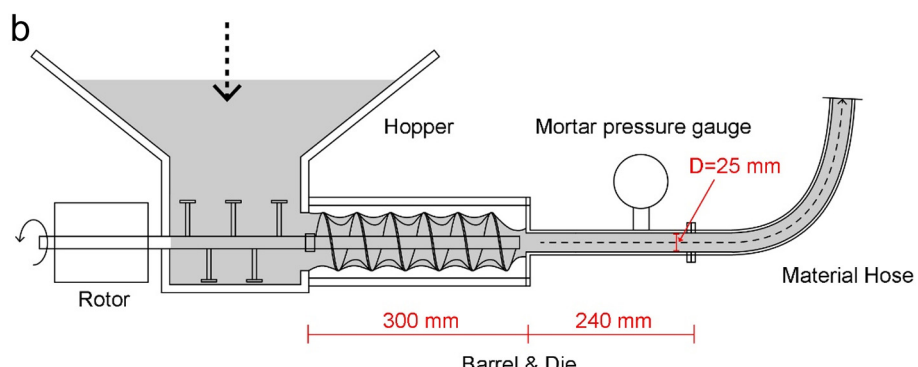
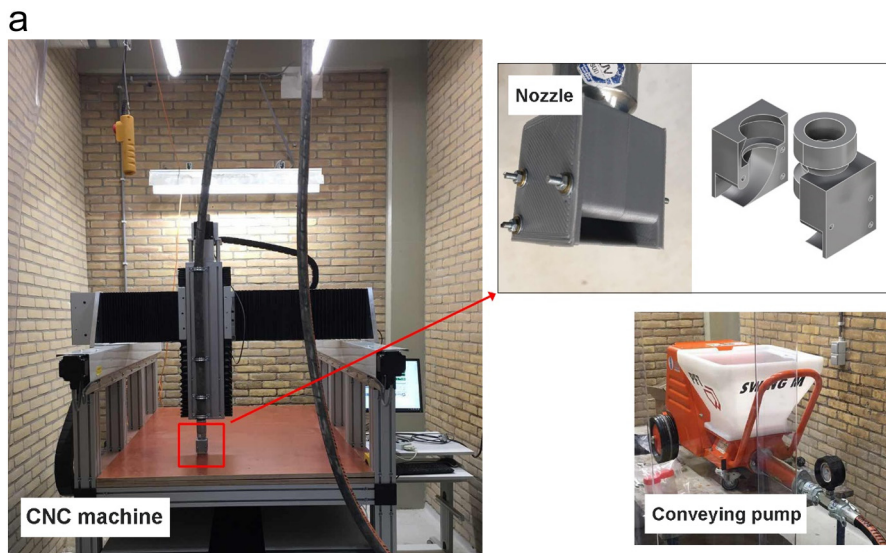


Fig. 4. (a) The 3DCP setup (CNC machine, conveying pump and nozzle) at Delft University of Technology; (b) Schematic diagram of PFT Swing-M conveying pump.

### 2.3. Test procedures

#### 2.3.1. Flowability test

Slump and slump flow tests were carried out to observe flowability changes of different mixtures after different resting times. The slump flow test was performed in accordance with ASTM C1437-15 [49]. A mini-cone mold with an upper internal diameter of 70 mm, a bottom internal diameter of 100 mm, and a height of 60 mm was used in this test. Before the test, the interior surface of the mold was lubricated by mold oil. One half of the mold was filled by the fresh mixture, and then the fresh mixture was agitated using a timber stick about 20 times. The same procedure was repeated for the second half of the mold. The excess material was slowly scraped off by a trowel. After removal of the mold, the height of the sample was measured. For the Ref mixture, the average diameter before dropping was measured instead of the height. Afterwards, the table was dropped 25 times within 25 s. The spread diameter was recorded through the measurement of four perpendicular directions. For each mixture, this test was performed for each material age from 10 min to 120 min, with intervals of 10 min. The fresh materials were sealed in a plastic bag to prevent evaporation of water. Three repetitions were conducted for each test.

#### 2.3.2. Extrudability test

For extrudability, the fresh mixture should be delivered through the nozzle continuously. The test was conducted on the 3DCP setup to determine the relationship between material flow rates and extrusion pressures for the mixtures containing VMA. 12 L of the fresh mixture were prepared according to track 2 (see Fig. 3) and then poured into the hopper of the pump. Different material flow rates ( $Q$ ) were applied through the controller of the pump. The pressures were recorded under different material flow rates. The test was performed at the material age of 10 min. According to Nerella et al. [7] and Tay et al. [50], the printing quality is also influenced by the nozzle moving speed. The linear material flow rate of a fresh mixture should be equal or larger than the moving speed of the printhead to ensure continuous printing. In this study, the nozzle moving speed was kept equal with the linear flow rate of the materials ( $Q$ ) that could be calculated through:

$$V_{\text{linear}} = \frac{Q}{A} \quad (1)$$

where  $Q$  and  $A$  represent the material flow rate (L/min) and the area of the nozzle opening ( $\text{mm}^2$ ).

#### 2.3.3. Open time test

Open time is defined as the time window of uninterrupted printing operation of a given volume of a mixture. The test method has been proposed in several earlier studies (see [15,51]). One filament (length: 800 mm and width: 40 mm) was printed at different material ages. The material flow rate and the nozzle moving speed were kept identical to the speeds of the extrudability test in Section 2.3.2. The test started at the resting time of 30 min with a time gap of 10 min, and it was not terminated until the disruption of filament occurred. To ensure that the fresh mixture remained in the dynamic state, a pre-pumping/shearing session was designed before printing the filament (see Fig. 5). Shape retention was checked by measuring the width of the printed segments using a vernier caliper. The shape retention ratio ( $S_1$ ) was introduced by Bong et al. [51] and Panda et al. [52] as:

$$S_1 = \frac{W_f}{W_n} \quad (2)$$

where  $W_f$  is the measured width of the extruded filament, and  $W_n$  is the width of the nozzle opening. The closer the value of  $S_1$  to 1, the better the shape retention.

#### 2.3.4. Buildability test

Due to the absence of formwork in the 3DCP process, the extruded

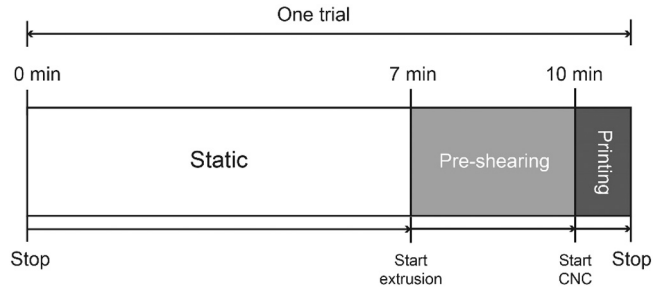


Fig. 5. Stages of a typical trial for printing a single filament.

cementitious filaments should have the ability to retain their shape under the self-weight and the loading from upper layers [9,28,35,38]. In this research, the assessment of buildability was based on the layer settlement test from Kazemian et al. [29]. One object containing five stacked layers was printed at a fixed time interval of about 40s. The nozzle standoff distance was kept as 0 mm during printing, which could ensure the same layer thickness of 13.5 mm. The five-layer object was designed to have 900 mm in length, 40 mm in width, and 67.5 mm in height. The test started at the material age of 30 min and finished before the end of open time. The printing speed (material flow rate and nozzle moving speed) was kept the same as the operation speeds used in extrudability and open time tests. The height of deposited layers ( $H$ ) was measured to calculate the shape stability ratio ( $S_2$ ) through:

$$S_2 = \frac{H}{h} \quad (3)$$

where  $h$  denotes the designed height of the five-layer object.

#### 2.3.5. Green strength test

The green strength test was performed to determine the strength development within the first 4 h for the mixtures incorporating VMA. The test procedure was the same as in the previous studies of the authors [13,53]. The fresh mixtures were prepared and then poured into cylindrical molds with a 33.5 mm internal diameter and 67.5 mm height. A silicon spray was initially used to coat the molds before filling the fresh mortar. All samples were compacted on a vibration table at a frequency of 30 Hz for 10s to reduce the amount of air bubbles. The samples were then stored in a sealed plastic bag and demolded right before the green strength testing. The Instron universal testing machine (8872), equipped with a 10 kN load cell, was used to perform the green strength tests. Both sides of a sample were covered by a double layer plastic film. In order to reduce the friction between the sample and base plates, Polytetrafluoroethylene was sprayed between two layers of plastic. The tests were performed using displacement control with a rate of 0.2 mm/s until reaching the maximum displacement of 20 mm. The entire test was recorded by a Canon camera model EOS 6D with a Tamron aspherical 28–75 mm lens. Vertical and lateral deformations of each sample were analyzed by a freeware image analysis software ImageJ. A MATLAB-code presented in [13] was employed to measure the change of cross-section of the sample. Each mixture was tested at the ages of 30, 45, 60, 90, 150, and 240 min. Three repetitions were conducted for each age. Table 3 provides the time specification of all fresh property tests in this study.

#### 2.3.6. Isothermal calorimetry test

An eight-channel TAM Air isothermal calorimeter was used to measure the heat flow from all of the mixtures in this study. Each channel contains two parallel cells, one for a testing vessel and the other for a reference vessel. 20 ml glass vessels were employed for the tested and reference samples. The reference vessel was filled with fine sand, which has a similar specific heat capacity as the tested sample. Each channel was an independent unit and was calibrated before starting the tests. The aggregate portion of each mix was excluded.

**Table 3**  
Time specification of fresh property tests.

Type	Material age	Test duration (per time)
Flowability test	10 min to 120 min (10 min of the time interval)	2–3 min
Extrudability test	30 min	10 min
Open time test	30 min to the terminated time (10 min of the time interval)	0.5–1 min
Buildability test	30 min	5 min
Green strength test	30, 45, 60, 90, 150, 240 min	2 min

Before placing the samples, a baseline was recorded for about 30 min. First, dry components were mixed manually with a blend of water and superplasticizer for about 2 min. Then, the pre-weighed VMA was added and dispersed in the suspension by mixing for 5 min. The samples with the same mass (6 g) were filled in the glass vessel and immediately moved into the calorimeter, which had been kept constantly at 20 °C. Heat values from the reactions of each mixture were recorded every 20 s for a period of 168 h (7 days).

### 2.3.7. Compressive strength test

The printed samples were sawn from the printed object that was manufactured in Section 2.3.4. Due to the anisotropic mechanical properties of the printed mortar [10,54,55], the printed samples were tested in X, Y, and Z direction (see Fig. 6), and the average value was calculated through 5 repeated tests in each direction. Thus, for each mixture, 15 printed samples were prepared and tested in total. The cast samples of mixture Ref were also prepared and tested. All samples had a dimension of 40 × 40 × 40 mm<sup>3</sup> and were cured in a fog room (20 ± 2 °C, 99% relative humidity). Compressive strength at 7 days was measured conforming NEN-EN 196-1 [56] at a loading rate of 2.4 kN/s.

### 2.3.8. X-ray computed tomography scanning

X-ray computed tomography (CT) scanning was used to investigate the air void content and distribution within samples printed using different mixtures. Small cylindrical samples with a 25 mm diameter and 24 mm height were drilled and sawn from the printed objects (From top to bottom: the second and third layers were sawn from the cored sample that contained 5 layers) in Section 2.3.4. A Phoenix Nanotom Micro CT-Scanner was used for scanning. 1441 images were acquired on a digital GE DXR detector (3072 × 2400 pixels). The theoretical spatial resolution was 13.3 × 13.3 × 13.3 μm<sup>3</sup>/voxel. The reconstruction was performed using the Phoenix Datas|x software. A cylindrical region of interest (ROI), which was selected at the area of the two-layer interface, was extracted from the sample for the air void analysis. The obtained

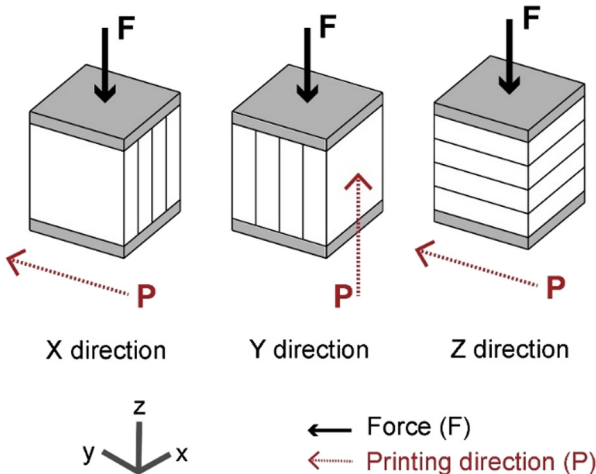


**Fig. 6.** Schematic diagram of loading directions for performing the compressive strength test on printed samples.

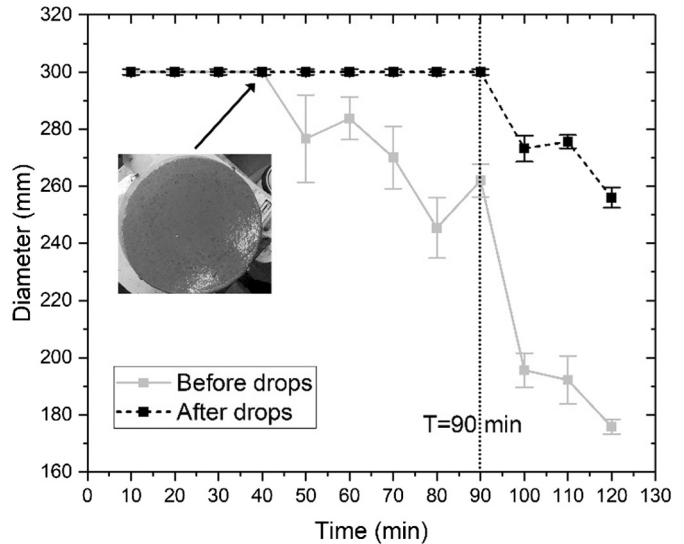


**Fig. 7.** The slump flow test results of mixture Ref.

image stack with the top view of the cylindrical ROI was analyzed via Trainable Weka Segmentation (TWS) from ImageJ (more information: [41,57]). The air voids from each image were isolated and measured.

## 3. Results

### 3.1. Flowability

Fig. 7 shows the results of the slump flow test of mixture Ref at different ages within the first 2 h. It could be recognized that the evident workability loss started after the resting time of 40 min. Between 50 min and 90 min, the spread diameter could still reach the value of 300 mm after the table dropped 25 times. However, after 90 min, a notable reduction in flowability was observed, which was likely due to the C-S-H bridges between particles forming a percolated rigid network in the material, as suggested by Roussel et al. [58]. This network of interacting particles is still fragile under a relatively high shear force. However, the table dropping process may not be able to supply sufficient shear energy to break all these inter-particle connections [37,58].

Fig. 8 provides the results of the slump and slump flow tests at different ages within the first 2 h. After a specific resting time, increasing the VMA dosage in the mixture could contribute to retaining the shape and height of the demolded sample. Mixture 4VMA showed nearly zero-slump (Fig. 8 (a)). All mixtures demonstrated enhanced shape stability with time. Compared with mixture 1.2VMA, mixture 2VMA presented slightly better shape retention before the age of 90 min. As shown in Fig. 8 (b), the spread diameter of all mixtures decreases with time. Thus, the workability of fresh mixtures decreases with increasing the resting time, which could be attributed to the gradual development of stiffness of the fresh mixture. Mixtures 1.2VMA and 2VMA demonstrated larger spread diameter at any specific age compared with mixture 4VMA. The effects on fluidity were not apparent when increasing the dosage of VMA from 0.14% to 0.24%.

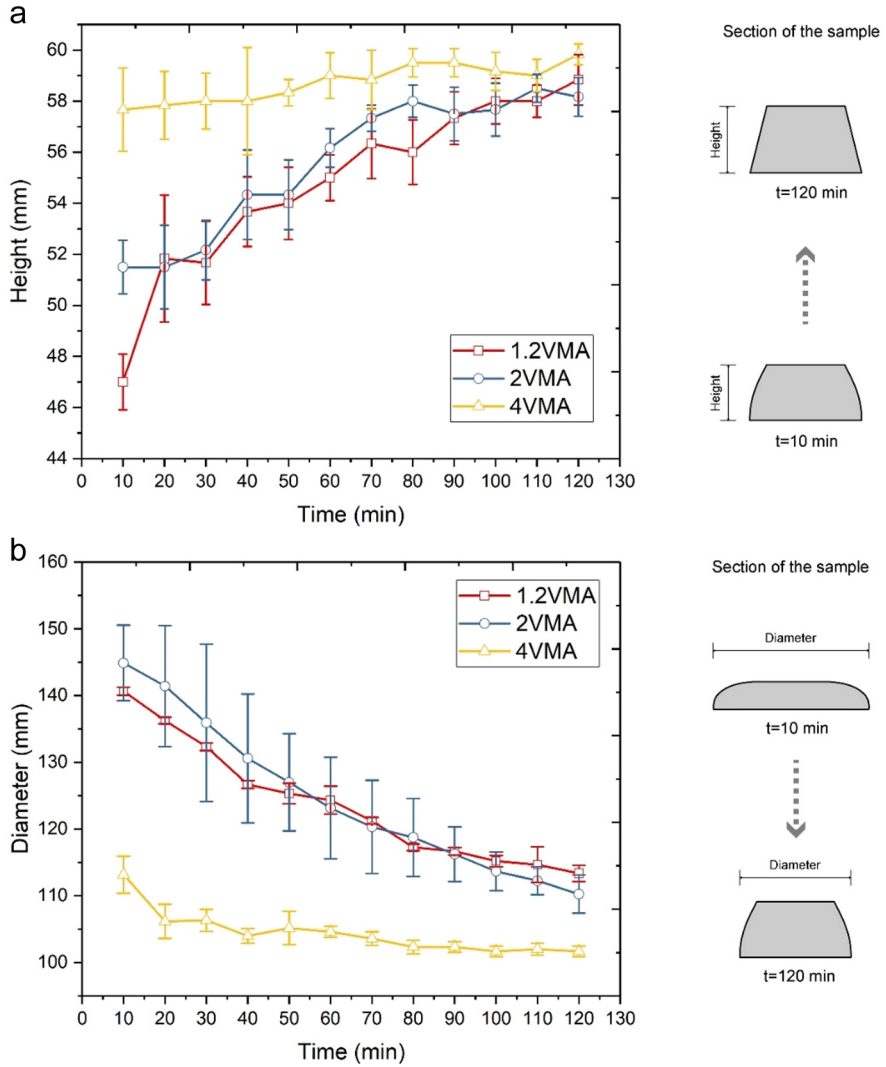


**Fig. 8.** Flowability test results of mixtures with different VMA contents: (a) Height (before dropping the table) and (b) Spread diameters (after dropping the table for 25 times) of demolded samples varied with different material ages.

However, once the VMA content reached 0.48%, the flowability of fresh mixture was significantly reduced.

### 3.2. Extrudability

Fig. 9 shows the results of extrudability tests of mixtures 1.2VMA, 2VMA, and 4VMA. With the increase of material flow rate, all mixtures lead to a larger extrusion pressure. A shear-thinning behavior for mixtures 1.2VMA and 2VMA can be recognized. It is evident that the mixture containing a higher dosage of VMA requires higher extrusion pressure to reach a similar material flow rate compared to mixtures containing lower dosages of VMA. A significant difference in extrusion pressure between 4VMA and 2VMA is quite clear. Due to the limitation of extrusion pressure (Maximum: 30 bar), mixture 4VMA could not be conveyed with  $> 0.65 \text{ L/min}$  of the material flow rate. The obtained results agree well with the ram extruder test results from Chen et al. [27]. The increased dosage of VMA could lead to the rise of the shear yield stress and flow consistency, which result in higher extrusion pressure. For mixtures 1.2VMA and 2VMA, a material flow rate of 1.45 L/min was selected to ensure the fresh mixture conveyed stable and consistently without surface ruptures. The nozzle moving speed was calculated according to Eq. (1) before performing the extrudability test. Finally, the nozzle moving speed was selected as 2700 mm/min for mixtures 1.2VMA and 2VMA and 1200 mm/min for mixture 4VMA.

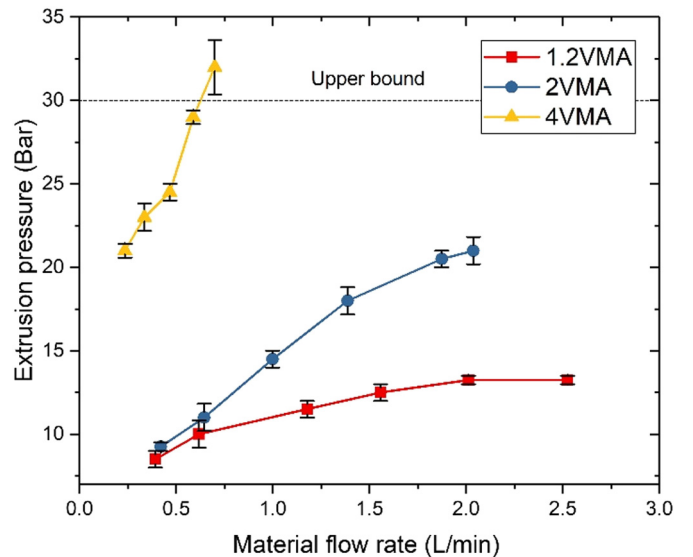


**Fig. 9.** The extrudability test results for mixtures 1.2VMA, 2VMA, and 4VMA. 1 bar = 0.1 MPa.

**Table 4**  
Open time of different mixtures.

Mixture	Open time (min)
1.2VMA	90
2VMA	70
4VMA	50

### 3.3. Open time

Results of the open time test are presented in Table 4 and Fig. 10. The filaments extruded at different ages were collected to demonstrate the change of printing quality with time. The open time for mixture 4VMA with the printing speed  $V_{p1}$  (material flow rate: 0.65 L/min; nozzle moving speed: 1200 mm/min) was found to be 50 min. The open time of 1.2VMA and 2VMA with the printing speed  $V_{p2}$  (material flow rate: 1.45 L/min; nozzle moving speed: 2700 mm/min) was found to be 90 min and 70 min, respectively. Besides, the width changes of the extruded filament with time are given in Fig. 11. Shape retention ratios ( $S_1$ ), calculated using Eq. (2), were employed to describe the accuracy of printing. Values of  $S_1 > 1$  were observed at a relatively early age since the fresh mixture showed low slump at the beginning. The extruded filament was thus wider than the nozzle opening. When  $S_1$  approached 1, the extruded filament presented a nearly accurate dimension. Values of  $S_1 < 1$  were caused by two factors. First, with the time passing, the material got stuck in the interior walls of the nozzle (see

Fig. 12), which led to thinner filaments. Second, the rheology of fresh mixtures was also changing with time due to the particle flocculation and nucleation process. Once the real material flow rate became much lower than the nozzle moving speed, the width of the filament was reduced, and disruption occurred.

### 3.4. Buildability and green strength development

Mixtures 1.2VMA, 2VMA, and 4VMA were used to print a five-layer object (see Fig. 13) with the time interval of 40 s (between two subsequent layers). The test session started at the material age of 30 min. Fig. 14 illustrates that shape stability could be enhanced by increasing the percentage of VMA from 0.14% to 0.48%. Mixture 4VMA showed the optimal buildability, and the value of  $S_2$  was close to 0.90. The shape stability of mixture 2VMA was very close to that of mixture 4VMA and much better than mixture 1.2VMA. The deformation of a sample printed using 1.2VMA was evidently larger than that of other mixtures. Fig. 14 also demonstrates that the cross-section of printed samples of 2VMA and 4VMA had similar bell shapes.

The green strength development within the first 4 h could be used as an indicator of the proper structural build-up of the mixture. With the help of ImageJ and a MATLAB code, the change of the cross-sectional area was recorded. The average strain/true stress curves of mixtures 1.2VMA, 2VMA, and 4VMA from the age of 30 min to 240 min are given in Fig. 15 (a)-(c). All curves for the 1.2VMA mixture showed a similar pattern. It has been observed that the stress linearly increased with the

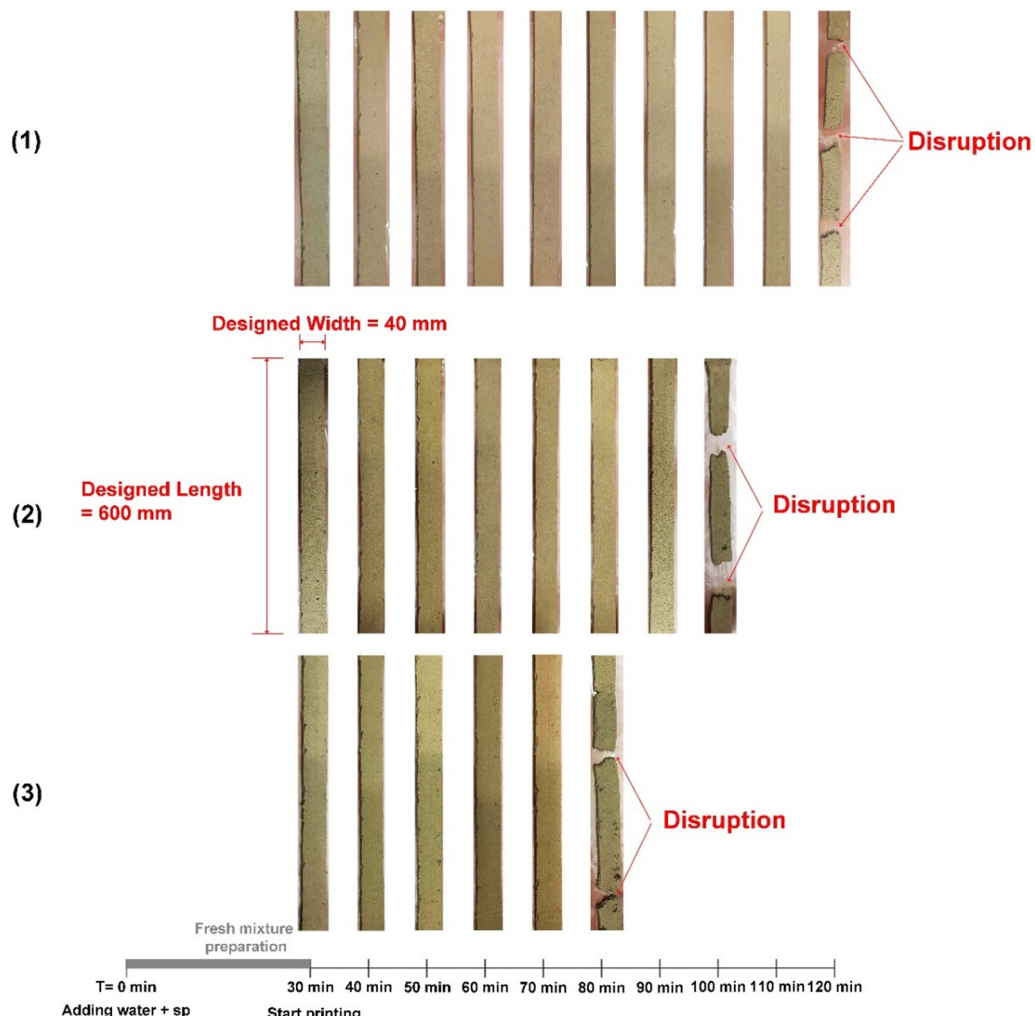


Fig. 10. Open time test results: (1) mixture 1.2VMA; (2) mixture 2VMA; (3) mixture 4VMA.

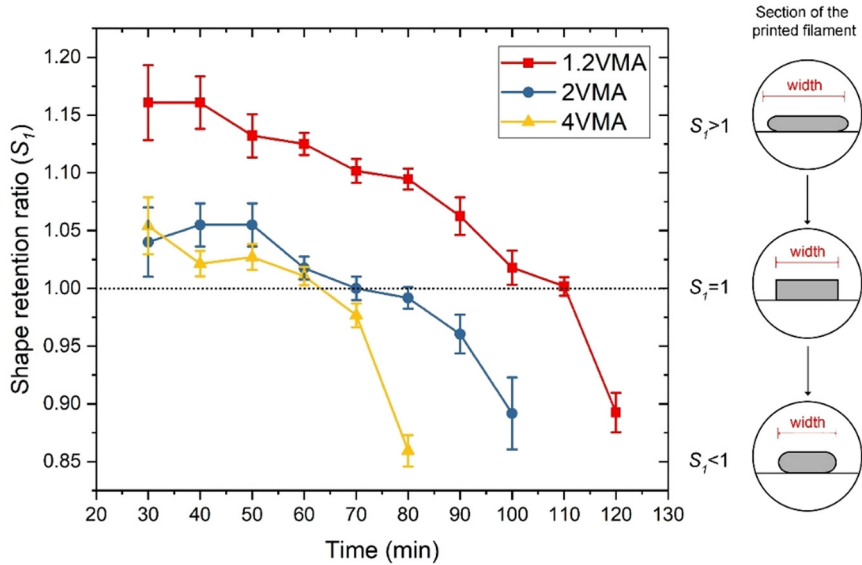


Fig. 11. Shape retention ratios of 1.2VMA, 2VMA, and 4VMA at different ages.



Fig. 12. The stiff material got stuck in the nozzle during the waiting period of the open time test, which is one of the reasons to restrict the printed amount.

growth of strain until to reach a certain plateau. For mixtures 2VMA and 4VMA, the samples with younger ages (30 min – 90 min) showed behavior similar to that of the mixture 1.2VMA, whereas older specimens (150 min – 240 min) showed strain softening after the peak value. Fig. 16 may explain this phenomenon. The samples with a resting time from 30 min to 90 min failed with a barreling effect. Distinct cracks could only be observed during testing of older samples (150 min – 240 min). This is in accordance with the published literature [13,34,59]. In Fig. 15 (d), green strength of each test (defined as the peak stress of each curve) is plotted. The average value of green strength and the Young's modulus are summarized in Table 5. Young's modulus was measured at 5% strain in this paper, as suggested by Wolfs et al. [34]. The green strengths of mixtures 2VMA and 4VMA within the first 4 h were quite close and much higher than mixture 1.2VMA. Mixture 4VMA showed a slightly higher value compared with the mixture 2VMA until the material age of 2.5 h.

### 3.5. Isothermal calorimetry

The normalized heat flow and cumulative heat results are given in Fig. 17. The results are plotted up to 7 days (168 h). It was found that

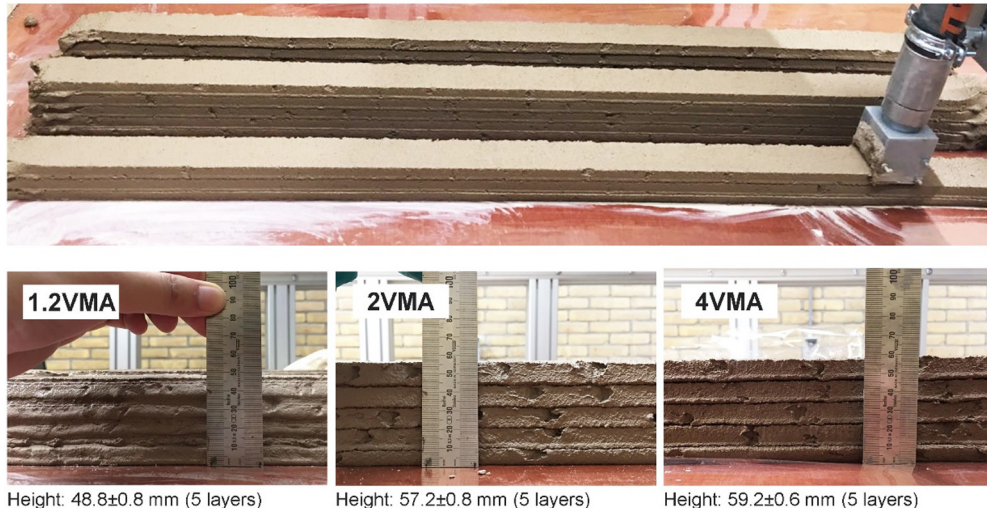
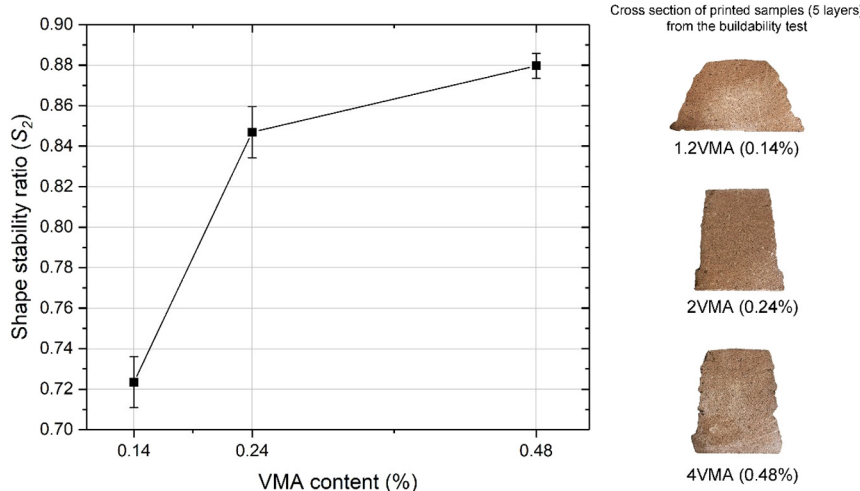


Fig. 13. Buildability tests of mixtures 1.2VMA, 2VMA, and 4VMA.



**Fig. 14.** Shape stability ratio of mixtures with different VMA contents (measured at 45 min of the resting time).

the normalized heat flow curve pattern of mixtures Ref, 1.2VMA, 2VMA, and 4VMA is almost the same in Fig. 17 (a). All of them showed the main hydration peak after the dormant period, a shoulder (second peak) that may be attributed to the depletion of sulfate, and a small slope (third peak) due to the formation of AFm phases [60]. With the increase of VMA dosage: (1) the reaction speed was slightly reduced in

the acceleration stage; (2) the time at which the main hydration peak occurs was delayed; (3) the intensity of the main hydration peak was decreased; (4) the intensity of the second peak was decreased, and less impact was observed on the third peak among mixtures containing VMA. As shown in Fig. 17 (b), the highest cumulative heat was released in mixture Ref, while the addition of VMA led to a decrease in the

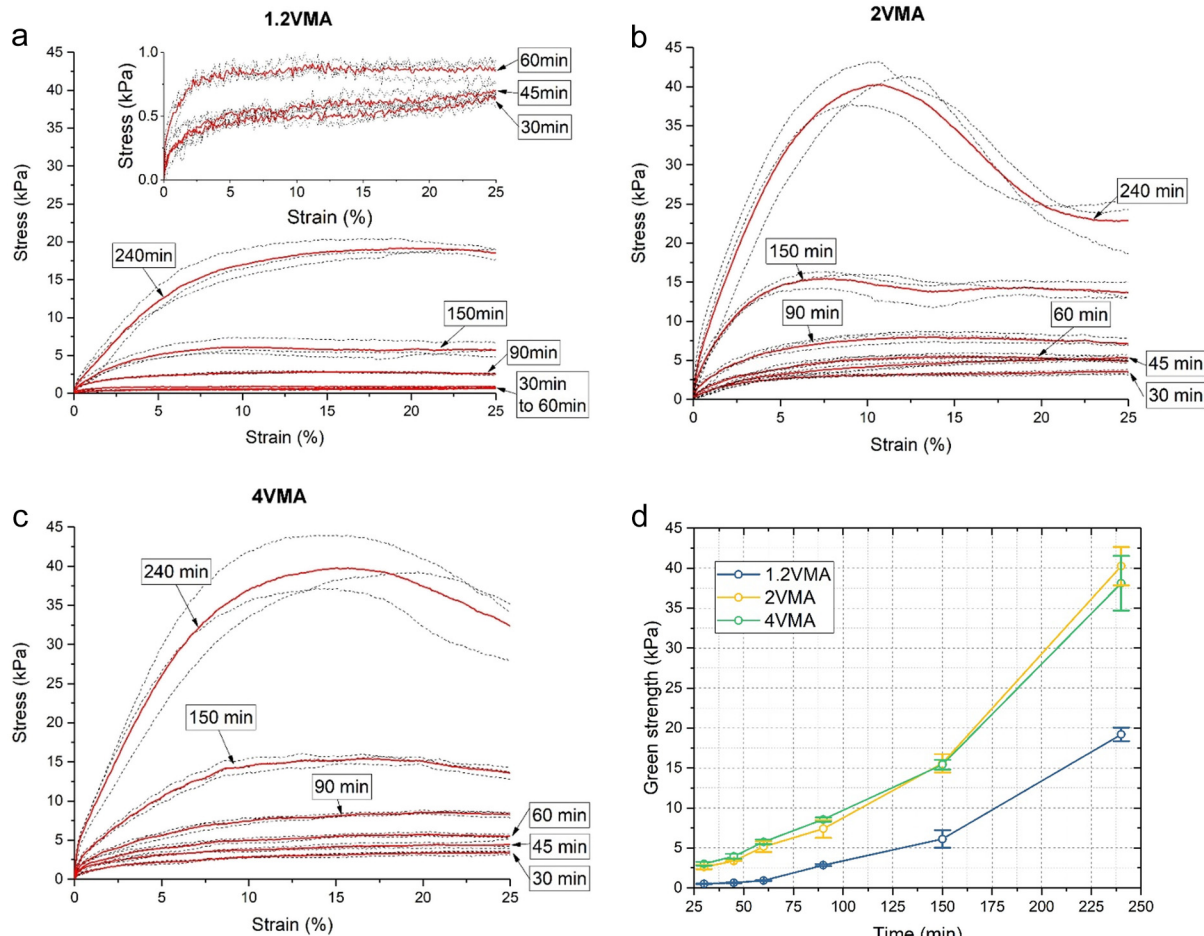


**Fig. 15.** (a) The stress/strain curve of mixture 1.2VMA; (b) The stress/strain curve of mixture 2VMA; (c) The stress/strain curve of mixture 4VMA. The black dashed lines indicate the individual test results, and the red curves represent the average stress and strain relation. (d) Comparison of green strength development of mixtures 1.2VMA, 2VMA, and 4VMA (error bars indicate standard deviation). (For interpretation of the references to colour in this figure legend, the reader is referred to the web version of this article.)

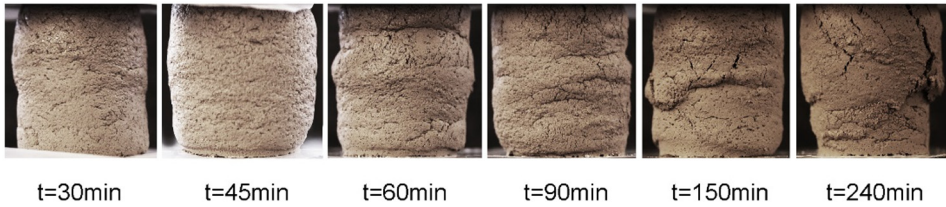


**Fig. 16.** Damaged samples of 2VMA at different material ages.

**Table 5**

The average value, standard deviation (SD), and relative standard deviation (RSD) of green strength ( $\sigma_G$ ), and Young's modulus ( $E_G$ ).

Time (min)	Green strength (kPa)			Young's Modulus (kPa)		
	$\sigma_G$	SD	RSD	$E_G$	SD	RSD
<b>1.2VMA</b>						
30	0.50	0.06	12.37%	8.62	0.44	5.06
45	0.63	0.03	5.04%	10.59	0.29	2.75
60	0.92	0.03	3.46%	16.58	1.14	6.87
90	2.84	0.12	4.38%	46.38	1.21	2.61
150	6.11	1.09	17.91%	102.03	13.13	12.87
240	19.19	0.85	4.45%	243.42	29.47	12.11
<b>2VMA</b>						
30	2.61	0.30	11.57	50.23	9.00	17.91
45	3.36	0.03	0.74	59.35	3.19	5.38
60	5.15	0.67	12.99	76.78	11.39	14.84
90	7.40	1.12	15.14	112.55	13.22	11.74
150	15.59	1.14	7.30	289.96	11.65	4.02
240	40.25	2.39	5.94	613.28	63.36	10.33
<b>4VMA</b>						
30	3.00	0.23	7.66	43.55	3.50	8.04
45	3.95	0.31	7.76	62.03	1.83	2.95
60	5.75	0.28	4.90	79.88	7.96	9.96
90	8.55	0.27	3.19	112.16	6.39	5.69
150	15.42	0.61	3.98	210.19	11.71	5.57
240	38.11	3.43	8.99	520.85	65.02	12.48

cumulative heat released in the first 7 days of hydration.

### 3.6. Compressive strength

Fig. 18 (a) shows the extracted areas from the printed objects that were made in Section 2.3.4. for preparing  $40 \times 40 \times 40 \text{ mm}^3$  samples. The test results of printed samples are presented in Table 6 and evaluated by analysis of variance (ANOVA) at 5% significance level shown in Table 7. The  $F$ -value of mixtures with different VMA content and different testing directions (X, Y, Z) are much larger than their corresponding  $F$ -critical values. The  $P$ -value in both sections is lower than 0.001. It means that both of them had a strong significance in the results. The ANOVA test confirms the statistical difference in the obtained results.

According to the test results shown in Fig. 18 (b), printed samples for all mixtures were stronger in the loading direction Y compared to X and Z directions (see Fig. 6). Similar compressive strength results of printed cementitious materials were reported by [55,61–63]. The distinct mechanical anisotropy of printed samples might be due to the weak interface and the printing quality. As explained by Panda et al. [63], the motion pattern of material in the printing process might be the main reason for the anisotropic property. The direction Y is the same as the direction of printing. Compared to the other directions (X and Z), the particles in the Y direction might be better placed and compacted. Besides, Nerella et al. [10] identified that the compaction due to the layer weight should also be taken into consideration for the variation of compressive strength. Mixture 2VMA showed the best compressive strength at 7 days in three different directions, compared with mixtures 1.2VMA and 4VMA. However, the mixtures modified by VMA exhibited lower compressive strength than mixture Ref, which agrees well with

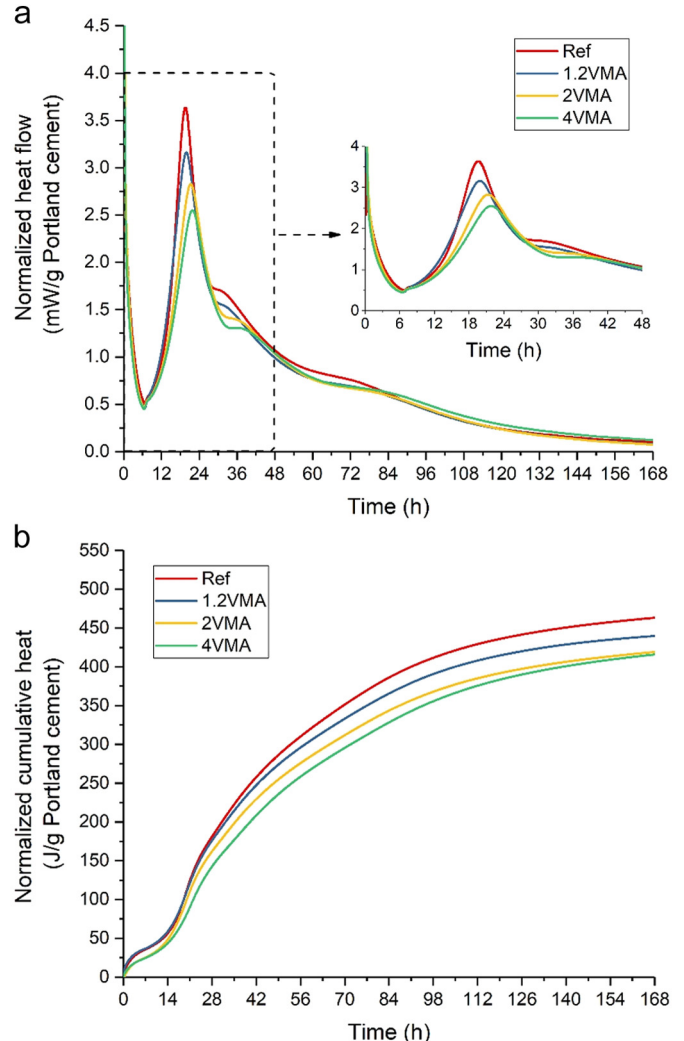


**Fig. 17.** Isothermal calorimetry test results: (a) Normalized heat flow with time, and (b) Normalized cumulative heat with time.

the result of isothermal calorimetry presented in Section 3.5.

### 3.7. X-ray computed tomography

The grayscale images obtained from CT scanning are shown in Fig. 19 (a). In all mixtures, the majority of large air voids can be observed in the interface region. 800 images in ROI from top to the bottom of the cylindrical sample were selected to measure the 2D void content using ImageJ, and the results are given in Fig. 19 (b). Air voids smaller than 5 pixels were neglected to avoid the effect of measurement noise. According to Fig. 19 (a), the interface of the sample 1.2VMA in the cross-section from the front view was of parabolic shape, unlike the relatively straight line in samples 2VMA and 4VMA. This is confirmed by the results presented in Fig. 19 (b). There are two peak values of sample 1.2VMA, which may be attributed to the weak buildability of

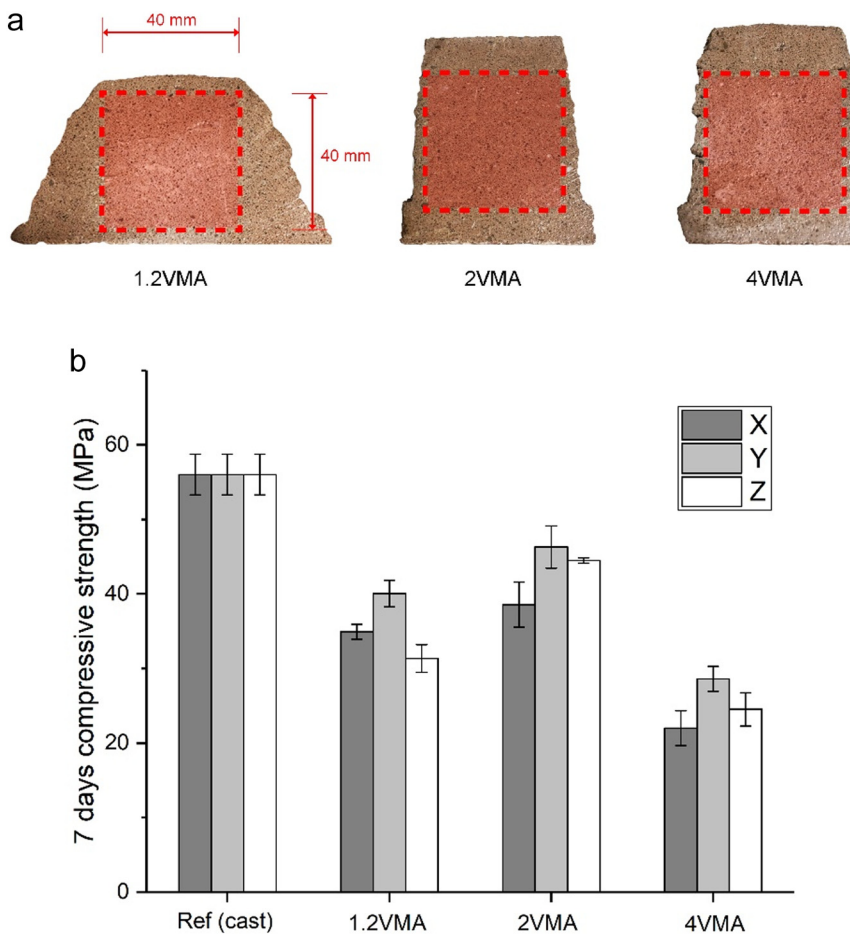


**Fig. 18.** (a) Extracted areas from the printed samples for performing compressive strength tests. (b) Compressive strength at the age of 7 days.

**Table 6**  
Compressive strength results of printed samples at 7 days.

Compressive strength at 7 days (MPa)			
	X	Y	Z
1.2VMA	33.373	37.822	29.577
	34.527	38.506	32.459
	34.802	41.833	32.327
	36.262	39.823	33.605
	35.693	42.37	28.756
	35.968	49.507	44.968
2VMA	36.903	45.227	44.574
	42.804	45.955	43.962
	38.616	49.078	44.455
	38.485	41.717	44.511
	18.8	28.717	23.892
4VMA	21.407	30.129	21.383
	22.63	30.519	26.547
	21.206	27.659	27.545
	25.971	25.991	23.277

the 1.2VMA mixture. The severe layer deformation that occurred during the printing process leads to the interface not being on the same horizontal plane. This is also visible in Fig. 14.

Compared with samples 2VMA and 4VMA, sample 1.2VMA contained a higher amount of relatively large air voids at the interface (see Fig. 19 (c)). However, sample 4VMA showed the highest cumulative void area around the interface. The number of large voids in sample 4VMA was not comparable with sample 1.2VMA based on visual inspection, whereas smaller pores were well-distributed in both the interface and the printed layers. Due to the limits in extrusion pressure, a lower printing speed was used for printing the sample of mixture 4VMA. The extruded filament of mixture 4VMA could therefore be less compacted than the others. Besides, many air voids remained and stabilized in the highly viscous cementitious materials during the mixing process [41,64]. That could be one of the reasons for the porous structure of the printed sample of mixture 4VMA in Fig. 19 (a).

Overall, the sample of mixture 2VMA displayed the densest microstructure and the smallest void content among all studied mixtures, which could explain why mixture 2VMA showed the highest compressive strength at 7 days (Section 3.6). However, it should be clarified

**Table 7**  
Analysis of variance (ANOVA) table for compressive strength results of printed samples.

Source of Variation	Sum of square mean	Degree of freedom	Mean Square	F-value	P-value	F-critical value
Different VMA content	2467.80	2	1233.90	257.53	< 0.001	3.26
Different test directions (X, Y, Z)	342.53	2	171.27	35.74	< 0.001	3.26
Interaction	124.82	4	31.21	6.51	< 0.001	2.63
Within	172.49	36	4.79			
Total	3107.65	44				

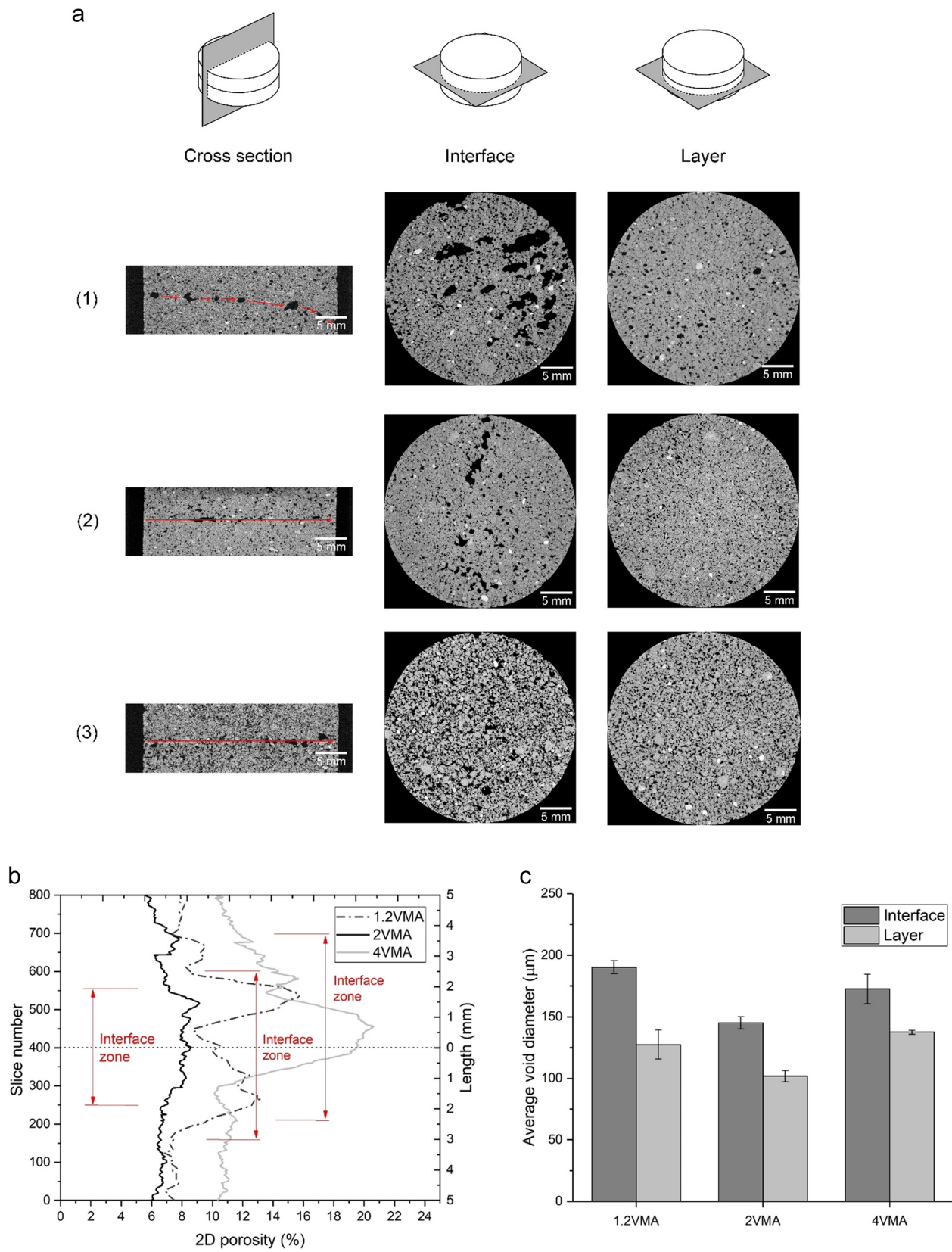


**Fig. 19.** (a) The grayscale images of the cross-section from the front view, the interface from the top view, and the layer from the top view: (1) Sample 1.2VMA; (2) Sample 2VMA; (3) Sample 4VMA. (b) 2D void content (porosity) from top to bottom of ROI; (c) The average air void diameter of the interface and layer.

that findings reported in this section are only based on one sample for each mixture. Further study is needed to ensure the accuracy and reliability of the findings.

## 4. Discussion

### 4.1. Effect of VMA dosage

#### 4.1.1. Flocculation and water retention

The competitive adsorption between PCE and HPMC has been confirmed by Ma et al. [65]. From a macroscopic point of view, the addition of cellulose-derivative VMAs could increase the plastic viscosity and/or yield stress for a fixed percentage of superplasticizer. For cellulose-derivative VMAs, a much more significant increase in plastic viscosity is seen than in yield stress [48,66]. At the microscale, two working mechanisms of VMA, i.e., flocculation and water retention, are emphasized in this study. The former describes the effects that appeared between fine particles, and the latter explains the function in the pore solution. In the presence of PCE, the possible flocculation mechanisms of VMA include bridging flocculation and depletion flocculation [67]. Both effects are dependent on the surface coverage condition of cement and other fine particles, and the competitive adsorption of PCE and HPMC.

On the other hand, HPMC could ‘arrest’ free water. The mechanism occurs because hydroxyl groups ( $-OH$ ), and ether groups ( $R-O-R$ ) can form the hydroxyl bond via combined water molecules. Therefore, the free water in suspension might be wrapped by the chain of HPMC, or be fixed outside of the structure [65]. As a result, the viscosity of the cement pore solution was increased by HPMC. Water retention increased with the molecular mass and the concentration of HPMC [48]. In this study, the water retention should be increased from 0.14% to 0.48% of HPMC dosage. The water retention of solid suspensions plays an important role in the formation of lubrication layers for concrete pumping and printing. More discussion about the lubrication layer is given in Section 4.1.3.

Overall, the discussion above might give the reason why mixture 4VMA exhibited extremely low flowability and high extrusion pressure compared with mixtures 2VMA and 1.2VMA. The function of VMA is strongly related to its concentration in the cement suspension. However, the role of calcined clay and limestone in the suspension system is not clear at present. This should be studied in the future.

#### 4.1.2. Retardation of hydration

The isothermal calorimetry test in Section 3.5 confirmed the retardation of cement hydration due to the addition of VMA in the limestone and calcined clay-based cementitious material system. The impact of cellulose-derivative VMAs on cement hydration has been reported by [41,48,68–70]. It has been found that the cellulose-derivative VMAs have very limited adsorption capability on anhydrous phases like  $C_3S$ , thus having less influence on the growth rate of C-S-H [48]. Many researchers [48,68,69] believe that the main reason for

delaying hydration by the cellulose-derivative VMAs is the adsorption onto hydrated phases, including C-S-H and portlandite. Pourchez et al. [69] explained that the cellulose-derivative VMAs acts strongly on the C-S-H precipitation by a three-step process: first, a reduction of the quantity of the initial C-S-H seeds; second, a retardation to form the C-S-H shell around the  $C_3S$ ; and finally, the formation of a thicker and permeable C-S-H layer. Additionally, the impacts on the second and third peaks by the addition of HPMC were also quite evident in Fig. 17 (a). Further tests, such as thermogravimetric analysis (TGA) and in-situ X-ray diffraction (XRD) measurements, are required to explain those phenomena.

#### 4.1.3. Lubrication layer and mechanical performance

Considering the retardation of hydration that occurs when using 0.48% of VMA (Fig. 17 (a)), it might be reasonable to expect that the mixture 4VMA will have the lowest compressive strength. However, the retardation of cement hydration were also quite evident when increasing the dosage of VMA from 0.14% to 0.24% (Fig. 17 (a)). Mixture 2VMA exhibited higher compressive strength in all directions compared to mixture 1.2VMA. A similar result was reported by Li et al. [38]. The authors explained that a thin water layer might be generated on the surface of the extruded filament by using the cement paste containing 0% or relatively small dosage of VMA. The weak bonding between two adjacent layers was due to that thin water layer.

The thin water layer could be regarded as one part of the lubrication layer. De Schutter and Feys [71] explained the formation of lubrication layer for the conventional pumpable concrete, such as self-compacting concrete. The authors point out that fresh concrete does not remain homogenous during pumping. Under the driving force, the coarse aggregate tends to move to the center of the unsheared region/plug-zone, whereas the cement paste and fine particles with the higher water content migrated to the pipe wall. For the laminar flow-based printing process, Roussel [37] indicated that only the water and the fine particles in the lubrication layer were sheared and play a function during pumping and extruding. The rheology of the unsheared region demonstrated minimal effects on extrusion but contributed more to the structural build-up process.

The free water content in the fresh mixture seems to play a dominant role in forming the lubrication layer. As mentioned in Section 4.1.1., free water content should be determined by the water retention properties induced by the VMA. The higher dosage of VMA results in higher water retention and less water mobility in the matrix, which raises difficulties in forming the lubrication layer. Once the lubrication layer was generated for mixtures containing a higher concentration of VMA, the formed layer showed very high viscosity, which could be proved by the increased extrusion pressure [37] (see Fig. 9). Finally, the lubrication layer remained on the surface of the extruded filament after deposition (Fig. 20). Hence, the adhesion between the two extruded layers was dependent on the rheological properties of the lubrication layers in the laminar flow based printing. The viscosity of the lubrication layer could not be too high or too low. The lubrication layer with a

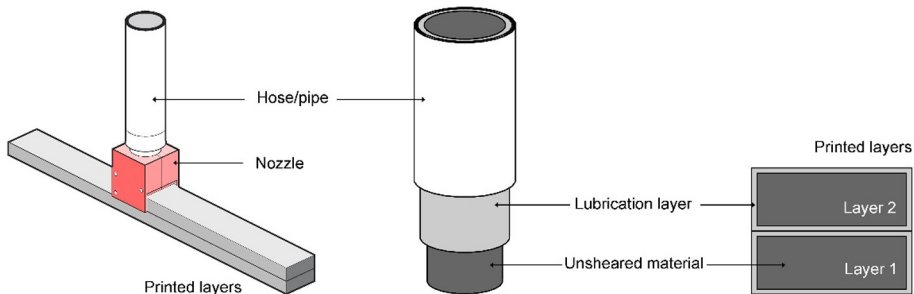


**Fig. 20.** Schematic of the laminar flow based printing (left). Formation of the lubrication layer in the material hose/pipe (middle). Section of two printed layers (right).

low viscosity might contain a higher water content which could increase the porosity in the interface like mixture 1.2VMA (see Fig. 19 (a), (b)). However, the opposite situation, such as mixture 4VMA, would lead to the extremely high extrusion pressure and the porous microstructure in both of the interface and the layer. Overall, the optimal value was found in the mixture 2VMA in this study.

#### 4.2. Limitations and perspective

##### 4.2.1. Nozzle moving speed and material flow rate

In this study, the default settings for extrudability and open time tests were to keep the nozzle moving speed the same as the linear material flow rate. However, as observed in the open time test (see Section 3.3.), the extruded filaments become thinner ( $S_1 < 1$ ) after a period of printing. As mentioned earlier, it could be seen that the stiff materials were stuck in the interior wall of the nozzle during the waiting period, and the rheology of the fresh mixture changed with time, which resulted in a decrease in the real material flow rate. There are two strategies to solve the latter problem in practice. First, using the optimized printability window. It is feasible to consume one batch of material before the time of appearance of the thinner filament by adjusting the printing speed and the maximum volume of one batch. For example, if the mixture 2VMA is to be printed, it must be ensured that a single batch of material is printed within 90 min. Second, using an inline monitoring and controlling system. It is also possible to decrease the nozzle moving speed or increase the material flow rate when the thinner filament appears. A real-time extrusion quality monitoring setup was proposed by Kazemian et al. [72]. The authors installed a camera on the printhead to collect the image data of the extruded filament. The width of the extruded filament was calculated and evaluated, and at the same time, a receipt (signal) was generated immediately. They developed a closed-loop extrusion system that could adjust the extrusion rate automatically based on the receipt from the quality monitoring system. It is possible to perform the precise printing work and extend the open time for the printable cementitious material by utilizing such a system.

##### 4.2.2. Object size and process

For a single printable cementitious material, its buildability and interlayer-bond strength could vary if the time interval between the two subsequent layers changes. In practice, for a constant printing speed, the time interval should be dependent on the path length of the layer. Thus, a large object would have a longer path length of the layer compared with a small object. Fig. 21 provides an example of the size effect of objects in the printing process. The stresses at 5% strain for mixture 2VMA during the resting time from 30 min to 90 min were collected from Table 5 and plotted in Fig. 21. A linear relationship between the material age and the stress could be achieved as well. It was recommended by Wolfs et al. [34] that the stress at 5% strain could provide a limit to ensure the geometrical accuracy of the printed objects. The grey line in Fig. 21 was defined as the strength evolution of the first layer (maximum strain: 5%). Three printing scenarios were proposed: large object, small object 1, and small object 2. All objects had the same default setup, including the nozzle opening (diameter: 15 mm), the printing speed (material flow rate: 1.1 L/min and nozzle moving speed: 3600 mm/min), the layer thickness (8 mm), the nozzle standoff distance (down-flow, 8 mm). The path length of each layer (for each object, the path length was kept the same from the bottom to the top) was 1200 mm and 7200 mm for two small objects and the large object, respectively. Fresh mixtures for both small objects were prepared at the same time. The main difference between them is the start time for printing.

In this case, the following assumptions are made: (1) The bottom layer was assumed to withstand only uniaxial compression that was due to the gravity-induced dead weight of the gradually increasing layers. (2) During the deposition process, the nozzle does not provide any

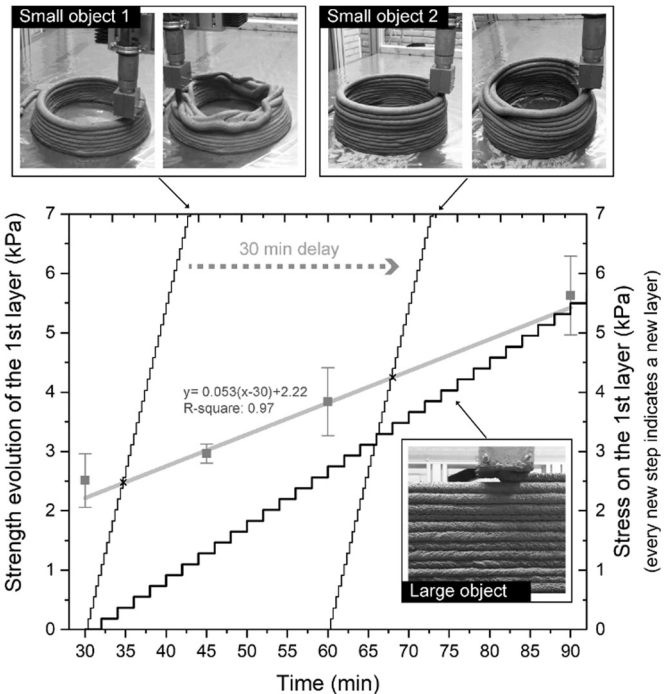


**Fig. 21.** The strength evolution of the bottom layer (the maximum strain: 5%) of mixture 2VMA during the period from 30 min to 90 min (grey line). Three printing scenarios: large object (start printing time: 30 min, path length of each layer: 7200 mm, computed layer number: 13, actual layer number: 9); small object 1 (start printing time: 30 min, path length of each layer: 1200 mm, computed layer number: 22, actual layer number: 15); small object 2 (start printing time: 60 min, path length of each layer: 1200 mm, computed layer number: 28, actual layer number: 21). Fresh mixtures for both small objects were prepared at the same time. Unit weight of mixture 2VMA: 2337 kg/m<sup>3</sup>; gravity constant: 9.8 N/kg.

stress on the layer. (3) 5% of the strain of the bottom layer was defined as the critical value before the printing failure. In practice, many other factors may lead to elastic buckling failure via the local or global instability of the printed structure, for instance, the object geometry, and imperfect layer deposition [33]. This was not considered in the current study.

As shown in Fig. 21, due to the prolonged time interval from 20s to 2 min, the large object was much more buildable than the small object 1. Thus, in this case, the mixture 2VMA may be more suitable to print the object with a relatively long time interval (> or = 2 min) between two subsequent layers. On the other hand, delaying the printing starting time in the small object 2 is a suitable strategy to increase the number of layers which can be printed, as shown by Li et al. [38]. The prolonged time interval was beneficial to reduce the deformation of the deposited layers and enhance the buildability, whereas it lowers the bond strength. Many studies [54,61,73,74] have already reported the reduction of interlayer strength due to the prolonged time gap. As mentioned by Perrot et al. [35] and Wangler et al. [75], for the fixed printing parameters (printing speed, layer thickness, nozzle, and others), the operation window of extrusion-based 3DCP depends on the structuration rate and the plastic viscosity of the printable mixtures.

##### 4.2.3. Relative printability

Due to the lack of standard protocols for evaluation of 3DCP [6,55], we attempted to formulate a test criterion to evaluate the printability of the developed limestone and calcined clay-based cementitious materials. Thus, the printability in this context should be defined as a relative result. As discussed earlier, except for the rheology of cementitious materials, the printability is related to the printing speed (nozzle moving speed and material flow rate), object size (path length of each

layer), object geometry, and the start printing time, among other parameters. Nevertheless, a developed cementitious material was printable using one printing setup, whereas it might be invalid or exhibit different behaviors using others. The printing system and process provide the upper and lower bounds for the printable cementitious materials. Therefore, development of printable cementitious materials cannot be seen as independent from 3DCP setup and the final application (object size and geometry). The final printing process should also fit the fresh state properties of the developed printable cementitious materials.

#### 4.2.4. Large-scale 3D concrete printing

Field application of 3DCP requires upscaling the printer setup and object from lab-scale to industrial-scale. Competing material properties determined at the lab-scale between pumpability and printability may be critically modified for manufacturing structural components or even complete buildings. To be pumpable, the fresh mixture must be fluid enough and should have a moderate yield stress and relatively low plastic viscosity [76]. The rheological properties should be very similar to self-compacting concrete during the pumping operation, which requires lower pumping pressure and is feasible for long-distance transportation. However, the fresh mixtures should show zero-slump after extrusion from the nozzle and then exhibit sufficient green strength to build the layered structure [77]. Many researchers aimed to achieve the rapid phase changing of fresh mixtures via rheology and/or hydration control. A concept was initially introduced by Gosselin et al. [78]: a pumpable mortar with the lower shear stress and slow hardening property was prepared and conveyed to the printhead which contained an inline mixer and extruder. At the same time, an accelerating admixture was injected into the printhead and dispersed in the fresh mortar. Thus, the setting of mortar was accelerated after deposition. A similar approach has also been reported by others [30,77,79].

Based on these studies [30,77–79], Fig. 22 presents a schematic diagram of a large-scale 3DCP system that can be potentially utilized for large-scale prefabrication or on-site construction. In Stage 1, the fresh mixture is prepared and pumped through a long hose ( $> 20$  m) to the construction site continuously. Once the low-viscosity material is collected in the inline mixer, activators such as accelerators, VMAs, and others can be delivered and mixed. Afterwards, the mixed materials are transported by an extruder. The requirements for the fresh mixture are as follows: (1) flowable and pumpable in Stage 1; (2) printable in Stage 2.

The developed mixtures in this study may be potentially used in the

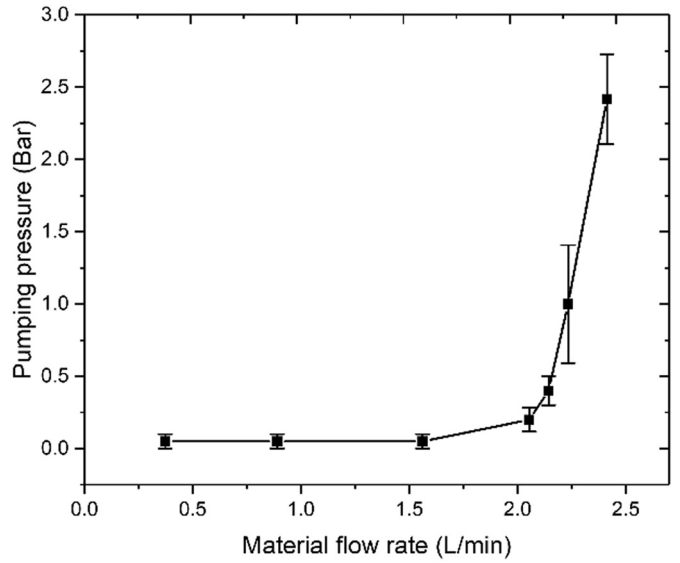


Fig. 23. The relationship between material flow rates and pumping pressures of mixture Ref. 1 bar = 0.1 MPa.

large-scale 3DCP system. A similar test as mentioned in Section 2.3.2. was also performed to determine the relationship between the material flow rate and the pumping pressures of mixture Ref. Pressurized bleeding and segregation were not observed during the test. The test result of mixture Ref is presented in Fig. 23. The pumping pressure shows a minimal and steady increase when the material flow rate is in the range of 0.35–2 L/min. After that, a much higher pumping pressure is needed for a small increment of material flow rate to 2 L/min. The shear-thickening property is observed by the increase in material flow rate from 2 to 2.4 L/min. Roussel et al. [80] explained that the macroscopic shear thickening behavior of cementitious materials occurs due to the particle inertia effects. The volume fraction of the solid suspension plays a dominant role in the shear-thickening behavior. Additionally, especially for highly flowable mixtures, the shear-induced particle migration could also be a reason for the shear-thickening phenomenon during the pumping process [81].

Overall, for stage 1, it would be possible to use the mixture Ref within a proper range of the material flow rate. However, for stage 2, the powdered VMA in this study may not be a good option since it needs several minutes to fully disperse in the fluid mixture. A liquid VMA

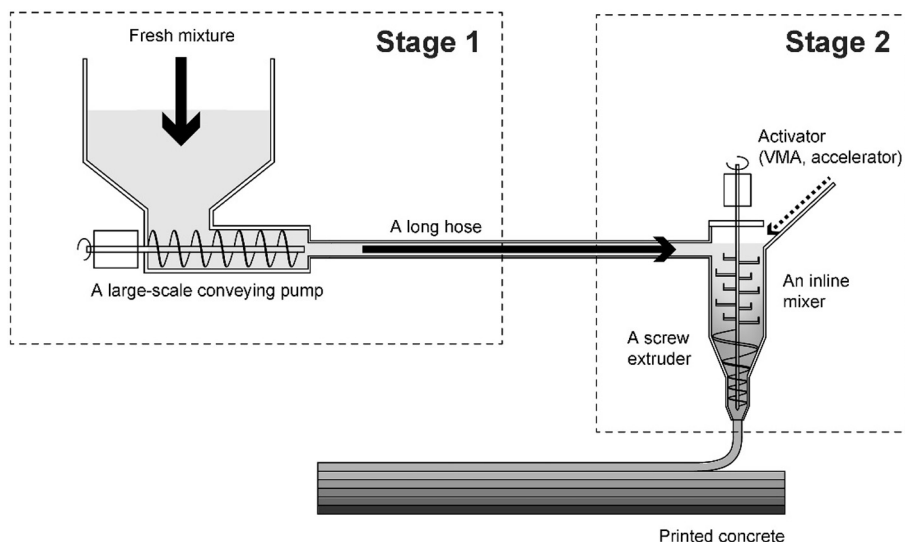


Fig. 22. A schematic diagram of the large-scale 3DCP system.

would be more suitable in this context. Also, since the limitations of the lab-scale printing setup, it is not feasible to validate if the developed mixtures could be directly used in the large-scale 3DCP system. Further validation is needed and will be carried out in the future.

## 5. Conclusion

The following conclusions could be obtained in this study:

- All mixtures containing VMA were printable through the 3DCP setup of TU Delft. Increasing the VMA dosage from 0.14% to 0.48% of the binder mass could increase the extrusion pressure, buildability, green strength within the first 2.5 h, and reduce the flowability and open time.
- Overall, the optimal VMA dosage for 3D printability is 0.24% of the binder mass (2VMA) in this study. Mixture 2VMA displayed better shape stability, buildability, and green strength than mixture 1.2VMA. Compared with mixture 4VMA, mixture 2VMA exhibited a more appropriate extrusion pressure, longer open time, comparable buildability and green strength.
- The addition and increase of VMA dosage in the mixture can retard the cement hydration. One possible reason is that the VMA might control C-S-H adsorption and massive portlandite precipitation.
- Anisotropy of the printed samples appears to be critical concerning compressive strength tests. For all mixtures, printed samples were stronger in the loading direction Y in comparison with directions X and Z. The mixture with 0.24% of VMA (2VMA) showed the best compressive strength at 7 days in all three directions. The effects induced by VMA addition can be attributed to the following reasons. First, the VMA addition could retard the hydration of the first 7 days. Second, for high viscosity material (4VMA), the air was entrapped and stabilized in the material during the mixing and printing processes. Third, in the laminar flow-based printing process, the composition (free water content) of the lubrication layer influenced the air void content between two layers. Water retention that was modified by VMA might be a critical factor in this aspect.
- For a precise printing process, it is important to keep the nozzle moving speed the same as the linear material flow rate by utilizing the optimized printability window and/or an inline monitoring and controlling system.
- Extending the time interval between two subsequent layers by increasing the object size (path length of each layer) could improve the buildability of printable materials, like mixture 2VMA. Delaying the start time is also a way to enhance the buildability for printable cementitious materials with sufficient open time. However, the weakness in bond strength when using mixture 2VMA to print large-scale objects is not clear so far and needs more investigation.
- The developed mixtures in this study can be potentially used in a large-scale 3DCP system. However, further research is required to validate this.

## Declaration of competing interest

On behalf of all the authors I declare that the content of this article is new and has not been published or submitted for publication elsewhere.

## Acknowledgments

Yu Chen, Zhenming Li, and Ze Chang would like to acknowledge the funding supported by China Scholarship Council under grant No. 201807720005, 201506120072, and 201806060129, respectively. The author would like to thank Dr. Branko Šavija for his suggestions and help. The authors appreciate Mr. Arjan Thijssen for his supports in the CT-scanning. Mr. Maiko van Leeuwen and Mr. Hugo Kuentz are also gratefully acknowledged for their help with the 3DCP experiments.

## References

- [1] J. Schwartz, Graphic statics and their potential for digital design and fabrication with concrete, *Cem. Concr. Res.* (2018), <https://doi.org/10.1016/j.cemconres.2018.06.015>.
- [2] G. De Schutter, K. Lesage, V. Mechtcherine, V.N. Nerella, G. Habert, I. Agusti-Juan, Vision of 3D printing with concrete — technical, economic and environmental potentials, *Cem. Concr. Res.* (2018), <https://doi.org/10.1016/j.cemconres.2018.06.001>.
- [3] ASTM, ASTM F2792-10, Standard Terminology for Additive Manufacturing Technologies, (2010), pp. 1–4, <https://doi.org/10.1520/F2792-12A.2>.
- [4] J.G. Sanjayan, B. Nematollahi, M. Xia, T. Marchment, Effect of surface moisture on inter-layer strength of 3D printed concrete, *Constr. Build. Mater.* (2018), <https://doi.org/10.1016/j.conbuildmat.2018.03.232>.
- [5] R.A. Buswell, W.R. Leal de Silva, S.Z. Jones, J. Dirrenberger, 3D printing using concrete extrusion: a roadmap for research, *Cem. Concr. Res.* (2018), <https://doi.org/10.1016/j.cemconres.2018.05.006>.
- [6] Y. Chen, F. Veer, O. Çopuroğlu, A critical review of 3D concrete printing as a low CO<sub>2</sub> concrete approach, *Heron* 62 (2017) 167–194.
- [7] V.N. Nerella, M. Näther, A. Iqbal, M. Butler, V. Mechtcherine, Inline quantification of extrudability of cementitious materials for digital construction, *Cem. Concr. Compos.* 95 (2019) 260–270, <https://doi.org/10.1016/j.cemconcomp.2018.09.015>.
- [8] S. Chaves Figueiredo, C. Romero Rodríguez, Z.Y. Ahmed, D.H. Bos, Y. Xu, T.M. Salet, O. Çopuroğlu, E. Schlangen, F.P. Bos, An approach to develop printable strain hardening cementitious composites, *Mater. Des.* 169 (2019), <https://doi.org/10.1016/j.matdes.2019.107651>.
- [9] T.T. Le, S.A. Austin, S. Lim, R.A. Buswell, A.G.F. Gibb, T. Thorpe, Mix design and fresh properties for high-performance printing concrete, *Mater. Struct. Constr.* 45 (2012) 1221–1232, <https://doi.org/10.1617/s11527-012-9828-z>.
- [10] V.N. Nerella, S. Hempel, V. Mechtcherine, Effects of layer-interface properties on mechanical performance of concrete elements produced by extrusion-based 3D-printing, *Constr. Build. Mater.* 205 (2019) 586–601, <https://doi.org/10.1016/j.conbuildmat.2019.01.235>.
- [11] T. Wangler, R. Roussel, F.P. Bos, T.A.M. Salet, R.J. Platt, Digital concrete: a review, *Cem. Concr. Res.* (2019), <https://doi.org/10.1016/j.cemconres.2019.105780>.
- [12] Y. Chen, F. Veer, O. Çopuroğlu, E. Schlangen, Feasibility of using low CO<sub>2</sub> concrete alternatives in extrusion-based 3D concrete printing, in: T. Wangler, R. Platt (Eds.), First RILEM Int. Conf. Concr. Digit. Fabr. – Digit. Concr., Springer, Cham, 2019, pp. 269–276, [https://doi.org/10.1007/978-3-319-99519-9\\_25](https://doi.org/10.1007/978-3-319-99519-9_25).
- [13] Y. Chen, Z. Li, S.C. Figueiredo, O. Copuroglu, F. Veer, E. Schlangen, Limestone and calcined clay-based sustainable cementitious materials for 3D concrete printing: a fundamental study of extrudability and early-age strength development, *Appl. Sci.* 9 (2019), <https://doi.org/10.3390/app9091809>.
- [14] B. Panda, C. Unluer, M.J. Tan, Investigation of the rheology and strength of geopolymer mixtures for extrusion-based 3D printing, *Cem. Concr. Compos.* 94 (2018) 307–314, <https://doi.org/10.1016/j.cemconcomp.2018.10.002>.
- [15] G. Ma, Z. Li, L. Wang, Printable properties of cementitious material containing copper tailings for extrusion based 3D printing, *Constr. Build. Mater.* 162 (2018) 613–627, <https://doi.org/10.1016/j.conbuildmat.2017.12.051>.
- [16] B. Panda, S. Ruan, C. Unluer, M.J. Tan, Improving the 3D printability of high volume fly ash mixtures via the use of nano attapulgite clay, *Compos. Part B Eng.* 165 (2019) 75–83, <https://doi.org/10.1016/j.compositesb.2018.11.109>.
- [17] J. Sanjayan, B. Nematollahi, M. Xia, L. Wang, M. Guowei, 3D concrete printing with low carbon cements, *Cem. Concr. Res.* (2020) (under review).
- [18] K. Scrivener, F. Martirena, S. Bishnoi, S. Maity, Calcined clay limestone cements (LC3), *Cem. Concr. Res.* 114 (2018) 49–56, <https://doi.org/10.1016/j.cemconres.2017.08.017>.
- [19] W. Huang, H. Kazemi-Kamyab, W. Sun, K. Scrivener, Effect of replacement of silica fume with calcined clay on the hydration and microstructural development of eco-UHPPRC, *Mater. Des.* 121 (2017) 36–46, <https://doi.org/10.1016/j.matdes.2017.02.052>.
- [20] Y. Dhandapani, T. Sakthivel, M. Santhanam, R. Gettu, R.G. Pillai, Mechanical properties and durability performance of concretes with limestone calcined clay cement (LC3), *Cem. Concr. Res.* 107 (2018) 136–151, <https://doi.org/10.1016/j.cemconres.2018.02.005>.
- [21] M. Antoni, J. Rossen, F. Martirena, K. Scrivener, Cement substitution by a combination of metakaolin and limestone, *Cem. Concr. Res.* 42 (2012) 1579–1589, <https://doi.org/10.1016/j.cemconres.2012.09.006>.
- [22] A. Tironi, A.N. Scian, E.F. Irassar, Blended cements with limestone filler and kaolinitic calcined clay: filler and Pozzolanic effects, *J. Mater. Civ. Eng.* 29 (2017) 04017116, [https://doi.org/10.1061/\(ASCE\)MT.1943-5533.0001965](https://doi.org/10.1061/(ASCE)MT.1943-5533.0001965).
- [23] G.L. Alvarez, A. Nazari, A. Bagheri, J.G. Sanjayan, C. De Lange, Microstructure, electrical and mechanical properties of steel fibres reinforced cement mortars with partial metakaolin and limestone addition, *Constr. Build. Mater.* 135 (2017) 8–20, <https://doi.org/10.1016/j.conbuildmat.2016.12.170>.
- [24] F. Avet, R. Snellings, A. Alujas Diaz, M. Ben Haha, K. Scrivener, Development of a new rapid, relevant and reliable (R3) test method to evaluate the pozzolanic reactivity of calcined kaolinitic clays, *Cem. Concr. Res.* 85 (2016) 1–11, <https://doi.org/10.1016/j.cemconres.2016.02.015>.
- [25] Y. Dhandapani, M. Santhanam, Assessment of pore structure evolution in the limestone calcined clay cementitious system and its implications for performance, *Cem. Concr. Compos.* 84 (2017) 36–47, <https://doi.org/10.1016/j.cemconcomp.2017.08.012>.
- [26] F. Avet, X. Li, K. Scrivener, Determination of the amount of reacted metakaolin in calcined clay blends, *Cem. Concr. Res.* 106 (2018) 40–48, <https://doi.org/10.1016/j.cemconres.2018.01.009>.
- [27] Y. Chen, S. Chaves Figueiredo, G. Yalçinkaya, O. Çopuroğlu, F. Veer, E. Schlangen, The effect of viscosity-modifying admixture on the extrudability of limestone and calcined clay-based cementitious material for extrusion-based 3D concrete printing,

- Materials (Basel) 12 (2019) 1374, <https://doi.org/10.3390/ma12091374>.
- [28] S. Lim, R.A. Buswell, T.T. Le, S.A. Austin, A.G.F. Gibb, T. Thorpe, Developments in construction-scale additive manufacturing processes, *Autom. Constr.* (2012), <https://doi.org/10.1016/j.autcon.2011.06.010>.
- [29] A. Kazemian, X. Yuan, E. Cochran, B. Khoshnevis, Cementitious materials for construction-scale 3D printing: laboratory testing of fresh printing mixture, *Constr. Build. Mater.* 145 (2017) 639–647, <https://doi.org/10.1016/j.conbuildmat.2017.04.015>.
- [30] L. Reiter, T. Wangler, N. Roussel, R.J. Flatt, The role of early age structural build-up in digital fabrication with concrete, *Cem. Concr. Res.* (2018), <https://doi.org/10.1016/j.cemconres.2018.05.011>.
- [31] A.V. Rahul, M. Santhanam, H. Meena, Z. Ghani, 3D printable concrete: mixture design and test methods, *Cem. Concr. Compos.* 97 (2019) 13–23, <https://doi.org/10.1016/j.cemconcomp.2018.12.014>.
- [32] H. Alghamdi, S.A.O. Nair, N. Neithalath, Insights into material design, extrusion rheology, and properties of 3D-printable alkali-activated fly ash-based binders, *Mater. Des.* (2019), <https://doi.org/10.1016/j.matdes.2019.107634>.
- [33] R.J.M. Wolfs, F.P. Bos, T.A.M. Salet, Triaxial compression testing on early age concrete for numerical analysis of 3D concrete printing, *Cem. Concr. Compos.* (2019), <https://doi.org/10.1016/j.cemconcomp.2019.103344>.
- [34] R.J.M. Wolfs, F.P. Bos, T.A.M. Salet, Early age mechanical behaviour of 3D printed concrete: numerical modelling and experimental testing, *Cem. Concr. Res.* 106 (2018) 103–116, <https://doi.org/10.1016/j.cemconres.2018.02.001>.
- [35] A. Perrot, D. Rangeard, A. Pierre, Structural built-up of cement-based materials used for 3D-printing extrusion techniques, *Mater. Struct.* 49 (2016) 1213–1220, <https://doi.org/10.1617/s11527-015-0571-0>.
- [36] D. Marchon, S. Kawashima, H. Bessaei-Bey, S. Mantellato, S. Ng, Hydration and rheology control of concrete for digital fabrication: potential admixtures and cement chemistry, *Cem. Concr. Res.* 112 (2018) 96–110, <https://doi.org/10.1016/j.cemconres.2018.05.014>.
- [37] N. Roussel, Rheological requirements for printable concretes, *Cem. Concr. Res.* (2018), <https://doi.org/10.1016/j.cemconres.2018.04.005>.
- [38] Z. Li, L. Wang, G. Ma, Method for the enhancement of buildability and bending resistance of 3D printable tailing mortar, *Int. J. Concr. Struct. Mater.* (2018), <https://doi.org/10.1186/s40069-018-0269-0>.
- [39] M. Palacios, R.J. Flatt, F. Puertas, A. Sanchez-Herencia, Compatibility between polycarboxylate and viscosity-modifying admixtures in cement pastes, *Am. Concr. Institute, ACI Spec. Publ.* (2012) 29–42.
- [40] M. Sonebi, A. Perrot, Effect of mix proportions on rheology and permeability of cement grouts containing viscosity modifying admixture, *Constr. Build. Mater.* (2019), <https://doi.org/10.1016/j.conbuildmat.2019.04.022>.
- [41] S. Chaves Figueiredo, O. Çopuroğlu, E. Schlangen, Effect of viscosity modifier admixture on Portland cement paste hydration and microstructure, *Constr. Build. Mater.* 212 (2019) 818–840, <https://doi.org/10.1016/j.conbuildmat.2019.04.020>.
- [42] A. Perrot, D. Rangeard, Y. Mélinge, Prediction of the ram extrusion force of cement-based materials, *Appl. Rheol.* 24 (2015), <https://doi.org/10.3933/APPLRHEOL-24-53320>.
- [43] L. Patural, P. Marchal, A. Govin, P. Grosseau, B. Ruot, O. Devès, Cellulose ethers influence on water retention and consistency in cement-based mortars, *Cem. Concr. Res.* (2011), <https://doi.org/10.1016/j.cemconres.2010.09.004>.
- [44] M. Chen, L. Li, Y. Zheng, P. Zhao, L. Lu, X. Cheng, Rheological and mechanical properties of admixtures modified 3D printing sulphoaluminato cementitious materials, *Constr. Build. Mater.* 189 (2018) 601–611, <https://doi.org/10.1016/j.conbuildmat.2018.09.037>.
- [45] D. Marchon, S. Mantellato, A.B. Eberhardt, R.J. Flatt, Adsorption of Chemical Admixtures, Elsevier Ltd, 2015, <https://doi.org/10.1016/B978-0-08-100693-1.00010-2>.
- [46] L. Lei, J. Plank, A study on the impact of different clay minerals on the dispersing force of conventional and modified vinyl ether based polycarboxylate superplasticizers, *Cem. Concr. Res.* (2014), <https://doi.org/10.1016/j.cemconres.2014.02.009>.
- [47] T. Kawai, T. Okada, Effect of Superplasticizer and viscosity-increasing admixture on properties of lightweight aggregate concrete, *ACI Symp. Publ.*, 119 1989, pp. 583–604, <https://doi.org/10.14359/2563>.
- [48] M. Palacios, R.J. Flatt, Working Mechanism of Viscosity-Modifying Admixtures, Elsevier Ltd, 2015, <https://doi.org/10.1016/B978-0-08-100693-1.00020-5>.
- [49] ASTM C1437-15, Standard Test Method for Flow of Hydraulic Cement Mortar, (2015), <https://doi.org/10.1520/C1437-15>.
- [50] Y.W.D. Tay, M.Y. Li, M.J. Tan, Effect of printing parameters in 3D concrete printing: printing region and support structures, *J. Mater. Process. Technol.* 271 (2019) 261–270, <https://doi.org/10.1016/j.jmatprotec.2019.04.007>.
- [51] S. Bong, B. Nematollahi, A. Nazari, M. Xia, J. Sanjayan, Method of optimisation for ambient temperature cured sustainable Geopolymers for 3D printing construction applications, *Materials (Basel)* 12 (2019) 902, <https://doi.org/10.3390/ma12060902>.
- [52] B. Panda, C. Unluer, M.J. Tan, Extrusion and rheology characterization of geopolymer nanocomposites used in 3D printing, *Compos. Part B Eng.* 176 (2019) 107290, <https://doi.org/10.1016/j.compositesb.2019.107290>.
- [53] Y. Chen, Ç. Yalçınkaya, O. Çopuroğlu, E. Schlangen, The effect of viscosity modifier agent on the early age strength of the limestone and Calcined clay-based sustainable and 3D printable Cementitious material, *Proc. 10th Int. Concr. Congr.*, Bursa Akademik Odalar Birliği, 2019, pp. 242–250 [https://www.researchgate.net/publication/332950478\\_The\\_Effect\\_Of\\_Viscosity\\_Modifier\\_Agent\\_On\\_The\\_Early\\_Age\\_Strength\\_OF\\_The\\_Limestone\\_And\\_Calcined\\_Clay-Based\\_Sustainable\\_And\\_3D\\_Printable\\_Cementitious\\_Material](https://www.researchgate.net/publication/332950478_The_Effect_Of_Viscosity_Modifier_Agent_On_The_Early_Age_Strength_OF_The_Limestone_And_Calcined_Clay-Based_Sustainable_And_3D_Printable_Cementitious_Material).
- [54] R.J.M. Wolfs, F.P. Bos, T.A.M. Salet, Hardened properties of 3D printed concrete: the influence of process parameters on interlayer adhesion, *Cem. Concr. Res.* 119 (2019) 132–140, <https://doi.org/10.1016/j.cemconres.2019.02.017>.
- [55] B. Panda, S.C. Paul, L.J. Hui, Y.W.D. Tay, M.J. Tan, Additive manufacturing of geopolymers for sustainable built environment, *J. Clean. Prod.* 167 (2017) 281–288, <https://doi.org/10.1016/j.jclepro.2017.08.165>.
- [56] NEN-EN 196-1, Methods of Testing Cement - Part 1: Determination of Strength, (2016).
- [57] I. Arganda-Carreras, V. Kaynig, C. Rueden, K.W. Eliceiri, J. Schindelin, A. Cardona, H.S. Seung, Trainable Weka segmentation: a machine learning tool for microscopy pixel classification, *Bioinformatics* 33 (2017) 2424–2426, <https://doi.org/10.1093/bioinformatics/btx180>.
- [58] N. Roussel, G. Ovarlez, S. Garrault, C. Brumaud, The origins of thixotropy of fresh cement pastes, *Cem. Concr. Res.* 42 (2012) 148–157, <https://doi.org/10.1016/j.cemconres.2011.09.004>.
- [59] B. Panda, J.H. Lim, M.J. Tan, Mechanical properties and deformation behaviour of early age concrete in the context of digital construction, *Compos. Part B Eng.* 165 (2019) 563–571, <https://doi.org/10.1016/j.compositesb.2019.02.040>.
- [60] F. Zunino, K.L. Scrivener, The influence of the filler effect in the sulfate requirement of OPC and blended cements, *Cem. Concr. Res.* 126 (2019) 105918, , <https://doi.org/10.1016/j.cemconres.2019.105918>.
- [61] T.T. Le, S.A. Austin, S. Lim, R.A. Buswell, R. Law, A.G.F. Gibb, T. Thorpe, Hardened properties of high-performance printing concrete, *Cem. Concr. Res.* (2012), <https://doi.org/10.1016/j.cemconres.2011.12.003>.
- [62] G. Ma, Z. Li, L. Wang, F. Wang, J. Sanjayan, Mechanical anisotropy of aligned fiber reinforced composite for extrusion-based 3D printing, *Constr. Build. Mater.* 202 (2019) 770–783, <https://doi.org/10.1016/j.conbuildmat.2019.01.008>.
- [63] B. Panda, G.B. Singh, C. Unluer, M.J. Tan, Synthesis and characterization of one-part geopolymers for extrusion based 3D concrete printing, *J. Clean. Prod.* 220 (2019) 610–619, <https://doi.org/10.1016/j.jclepro.2019.02.185>.
- [64] A. Jenni, L. Holzer, R. Zurbriggen, M. Herwegh, Influence of polymers on microstructure and adhesive strength of cementitious tile adhesive mortars, *Cem. Concr. Res.* 35 (2005) 35–50, <https://doi.org/10.1016/j.cemconres.2004.06.039>.
- [65] B. Ma, Y. Peng, H. Tan, S. Jian, Z. Zhi, Y. Guo, H. Qi, T. Zhang, X. He, Effect of hydroxypropyl-methyl cellulose ether on rheology of cement paste plasticized by polycarboxylate superplasticizer, *Constr. Build. Mater.* 160 (2018) 341–350, <https://doi.org/10.1016/j.conbuildmat.2017.11.010>.
- [66] K.H. Khayat, N. Milkovic, Viscosity-Enhancing Admixtures and the Rheology of Concrete, Woodhead Publishing Limited, 2011, <https://doi.org/10.1016/B978-0-85709-028-7.50008-X>.
- [67] R.J. Flatt, Impact of Concrete Admixtures on Concrete Rheology, Presented at the PhD Course on Rheology of Concrete and Cement-Based Materials, Dresden, (2019).
- [68] J. Pourchez, A. Peschard, P. Grosseau, R. Guyonnet, B. Guilhot, F. Vallée, HPMC and HEMC influence on cement hydration, *Cem. Concr. Res.* 36 (2006) 288–294, <https://doi.org/10.1016/j.cemconres.2005.08.003>.
- [69] J. Pourchez, P. Grosseau, B. Ruot, Changes in C3S hydration in the presence of cellulose ethers, *Cem. Concr. Res.* 40 (2010) 179–188, <https://doi.org/10.1016/j.cemconres.2009.10.008>.
- [70] Z.H. Ou, B.G. Ma, S.W. Jian, Influence of cellulose ethers molecular parameters on hydration kinetics of Portland cement at early ages, *Constr. Build. Mater.* 33 (2012) 78–83, <https://doi.org/10.1016/j.conbuildmat.2012.01.007>.
- [71] G. De Schutter, D. Feys, Pumping of fresh concrete: insights and challenges, *RILEM Tech. Lett.* 1 (2016) 76, <https://doi.org/10.21289/rilemtechlett.2016.15>.
- [72] A. Kazemian, X. Yuan, O. Davtalab, B. Khoshnevis, Computer vision for real-time extrusion quality monitoring and control in robotic construction, *Autom. Constr.* (2019), <https://doi.org/10.1016/j.autcon.2019.01.022>.
- [73] B. Panda, S.C. Paul, N.A.N. Mohamed, Y.W.D. Tay, M.J. Tan, Measurement of tensile bond strength of 3D printed geopolymer mortar, *Meas. J. Int. Meas. Confed.* 113 (2018) 108–116, <https://doi.org/10.1016/j.measurement.2017.08.051>.
- [74] Y.W.D. Tay, G.H.A. Ting, Y. Qian, B. Panda, L. He, M.J. Tan, Time gap effect on bond strength of 3D-printed concrete, *Virtual Phys. Prototyp.* 14 (2019) 104–113, <https://doi.org/10.1080/17452759.2018.1500420>.
- [75] T. Wangler, E. Lloret, L. Reiter, N. Hack, F. Gramazio, M. Kohler, M. Bernhard, B. Dillenburger, J. Buchli, N. Roussel, R. Flatt, Digital concrete: opportunities and challenges, *RILEM Tech. Lett.* 1 (2016) 67, <https://doi.org/10.21289/rilemtechlett.2016.16>.
- [76] V.N. Nerella, V. Mechtherine, Studying the printability of fresh concrete for formwork-free concrete onsite 3D printing technology (CONPrint3D), *3D Concr. Print. Technol.*, Elsevier Inc, 2019, pp. 333–347, , <https://doi.org/10.1016/b978-0-12815481-6.00016-6>.
- [77] T. Wangler, Digital concrete: Research and applications, *Proc. 10th Int. Concr. Congr.*, 2019, pp. 2–12.
- [78] C. Gosselin, R. Duballet, P. Roux, N. Gaudilliére, J. Dirrenberger, P. Morel, Large-scale 3D printing of ultra-high performance concrete - a new processing route for architects and builders, *Mater. Des.* 100 (2016) 102–109, <https://doi.org/10.1016/j.matecdes.2016.03.097>.
- [79] V. Esnault, A. Labyad, M. Chantin, F. Toussaint, Experience in online modification of rheology and strength acquisition of 3D printable mortars, in: T. Wangler, R. Flatt (Eds.), First RILEM Int. Conf. Concr. Digit. – Digit. Concr., Springer International Publishing, 2019, pp. 24–38, , [https://doi.org/10.1007/978-3-319-99519-9\\_3](https://doi.org/10.1007/978-3-319-99519-9_3).
- [80] N. Roussel, A. Lemaitre, R.J. Flatt, P. Coussot, Steady state flow of cement suspensions: a micromechanical state of the art, *Cem. Concr. Res.* 40 (2010) 77–84, <https://doi.org/10.1016/j.cemconres.2009.08.026>.
- [81] M. Choi, N. Roussel, Y. Kim, J. Kim, Lubrication layer properties during concrete pumping, *Cem. Concr. Res.* 45 (2013) 69–78, <https://doi.org/10.1016/j.cemconres.2012.11.001>.